JOURNAL OF SPACECRAFT AND ROCKETS
Vol. 29, No. 1, January–February 1992

New Technique for Low-to-High Altitude Predictions of Ablative Hypersonic Flowfields

Bilal A. Bhutta* and Clark H. Lewis†
VRA, Inc., Blacksburg, Virginia 24063

A new coupled-chemistry PNS solution technique is developed for predicting finite-rate chemically reacting flows over a wide range of Mach numbers and for altitudes ranging from sea level to 250 kft. New diagonalized, two-step, and strongly implicit solution schemes are developed to efficiently and accurately solve the coupled species conservation equations. Furthermore, a new quasisteady ablation model is developed for Teflon that accounts for the material density variations. Numerical tests are conducted over the Mach number range of 6.89–20 and altitude range from sea level to 250 kft, and comparisons are made with available wind-tunnel and flight data on surface heat-transfer rates. The results show that the new two-step solution scheme provides a uniquely attractive combination of accuracy, stability, and computational efficiency over the entire range of conditions tested. Furthermore, nonablating low-altitude calculations show that finite-rate chemistry effects are still significant over a major portion of the shock layer. The classical Blottner-type linearization of the production terms is unstable for low-altitude high-Reynolds-number conditions. The results of Teflon ablation calculations show that, for the altitude range of 75–250 kft, the predicted surface ablation rates using our quasisteady ablation model are within 10% of the predictions of Scala's correlation based on flight data.

Nomenclature

CI, C_i	= mass fraction of ith species
C_p	= specific heat at constant pressure
D_{ij}	= diffusion coefficient for the ith species with respect to the jth species
EI, E_e	= mass fraction of eth element
h	= static enthalpy
J	= determinant of the transformation Jacobian
$(J_i)_j$	= diffusion mass flux, $(Le\bar{\mu}/Pr)(C_i)_{,x_j}$
K_b	= backward reaction rate
K_c	= equilibrium constant
K_f	= forward reaction rate
k_i	= thermal conductivity of ith species
Le	= binary Lewis number, $\rho^*\bar{C}_p^*D_{ii}^*/\bar{k}^*$
L_i	= log of the molar concentration of ith species, $\rho C_i/M_i$
$LMAX$	= number of grid points in the ξ_2 direction
M	= Mach number
M_i	= molecular weight of ith species
$MDOT$, $\dot{m}$	= surface ablation rate, $(\rho w)_w/\rho_\infty V_\infty$
m	= molecular weight
m_{2kk}	= $\xi_{2,x}\xi_{2,x} + \xi_{2,y}\xi_{2,y} + \xi_{2,z}\xi_{2,z}$
NE	= total number of elements
NM	= total number of group 1 species
NS	= total number of chemical species
NZ	= total number of chemical third bodies
n	= iteration number
Pr	= Prandtl number
p	= static pressure
QW	= total wall heat-transfer rate
R	= radial distance from body axis
RB	= local body radius
Re	= Reynolds number, $(\rho^*V^*Rn^*)/\mu^*$
RN, Rn	= nose radius
T	= static temperature
$TINF$	= freestream static temperature, T_∞
U_j	= contravariant velocity, $u\xi_{j,x} + v\xi_{j,y} + w\xi_{j,z}$
u	= x component of mass-averaged velocity
V	= total mass-averaged velocity
v	= y component of mass-averaged velocity
w	= z component of mass-averaged velocity
X, x	= coordinate along body axis
Y	= y coordinate
Z	= z coordinate
ϵ	= M_∞/Re_∞
ξ_1	= marching or streamwise coordinate
ξ_2	= coordinate measured from the body to the outer bow shock
ξ_3	= crossflow coordinate
ρ	= mixture density
ω	= under-relaxation factor
$\dot{\omega}_i$	= production rate of the ith species

Subscripts

a	= amorphous Teflon
i	= ith chemical species or in-depth conditions
s	= solid Teflon
w	= wall quantity
,	= partial derivative
∞	= freestream quantity

Superscripts

EQ	= equilibrium conditions
j	= index in ξ_1 direction
n	= index for iteration
T	= vector or matrix transpose
*	= dimensional quantity
–	= mixture property

Introduction

THE baseline parabolized Navier-Stokes (PNS) scheme used in this study has been developed by the authors over the past several years[1–12] and uses a uniquely accurate solution scheme (free of any sublayer-type approximation[10,11]) along with an iterative numerical technique based on a pseudo-unsteady approach to the final steady-state solution. Although even the scalar computational times for a typical decoy-type re-entry calculation with this PNS scheme are very fast, significant headway has also been made to completely vectorize the

Received July 24, 1991; revision received Oct. 17, 1991; accepted for publication Oct. 18, 1991.

*Chief Scientist. Senior Member AIAA.
†President. Associate Fellow AIAA.

solution scheme. Tests have shown that even without complete vectorization, this nonequilibrium PNS scheme with a complex Teflon-air chemical system is actually more than an order of magnitude faster than a state-of-the-art finite difference nonequilibrium boundary-layer code (NEBL code of Finson et al.[13]). In fact, this comparison does not even include the significant amount of additional time required by the boundary-layer scheme to do the nonequilibrium edge conditions. On the other hand, the nonequilibrium PNS scheme is not only faster but also more accurate and consistent, and complete second-order effects (displacement thickness, vorticity interaction, and transverse and longitudinal curvature) are included.

The main objective of this paper is to present a new PNS technique for predicting chemically reacting re-entry flowfields over a wide range of altitudes ranging from sea level to 250 kft. For simplicity, the present study focuses on axisymmetric flows; however, subsequent extensions to three-dimensional flows and/or other chemical systems are also relatively straightforward. The various results obtained thus far in this study show that this nonequilibrium coupled-chemistry PNS scheme can indeed provide a good combination of prediction accuracy, simplicity, and computational speed.

In general, in this study, we have incorporated a general nonequilibrium and near-equilibrium flow modeling capability in our nonequilibrium PNS afterbody solution schemes. The nonequilibrium solution scheme used is also stable in the equilibrium (infinite reaction rate) and frozen (zero reaction rate) limits. Typically, for equilibrium or near-equilibrium flows, the species conservation equations become numerically stiff and must be solved in a mutually coupled manner.[14] Different workers have used different forms of this coupling. Finson and Ameer[15] used a temperature and species coupling, whereas Li[16] has shown that only a species coupling can also be adequate to resolve the associated problem of numerical stiffness. We believe that the temperature-species coupling can be important in the blunt-body region, whereas the species coupling will be adequate in the afterbody region. Indeed, the results of this study do substantiate this approach.

In this study we have considered three types of numerical solution schemes for solving the nonequilibrium species conservation equations: 1) a strongly implicit solution scheme, 2) a two-step solution scheme, and 3) a diagonalized solution scheme. Furthermore, the present study focuses on clean-air and ablative Teflon-air chemical systems. Several test cases have been computed to demonstrate the feasibility and evaluate the accuracy of the new strongly implicit as well as two-step coupled-chemistry PNS solution schemes. The results obtained are indeed quite encouraging and show that the new two-step solution approach for solving the species conservation equations is very attractive because it not only avoids the numerical stiffness problem but also is the most efficient in terms of computational speed.

Teflon-Air Chemical Model

Teflon (C_2F_4) is a fluorocarbon polymer compound most commonly used as a low-temperature ablator for heat-shield applications and for the purpose of shock-layer electron quenching. The oxidation and reduction chemistry of C_2F_4 is not very well understood. The possible species from the oxidation, reduction, and ionization of a system composed of F, C, N, and O can be numerous.[17] Some of the species can be identified as trace, whereas the reaction mechanisms of some species are not even well understood. In this study, both clean-air and Teflon-air gas mixtures are considered; however, since the clean-air system is a subset of the Teflon-air system discussed later, it is not addressed separately.

The present Teflon-air chemical model is based on the data used by Bhutta and Lewis,[5] Bhutta et al.,[6] and Blottner et al.[18] In this chemical model, Na and Na^+ were included to simulate the effects of sodium contamination on the ablation products. The overall Teflon-air chemical system used consists of 23 species (O, O_2, N, N_2, NO, C, C_2, C_3, CO, CO_2, Na, F, F_2, CF_2, CF_4, COF_2, C_2F_4, NO^+, O^-, O_2^-, Na^+, F^-, and e^-) and 36 gas-phase reactions. The gas-phase reactions and associated forward reaction rates are given in Table 1. The first seven of these reactions are based on the seven-species nonequilibrium-air work of Blottner et al.[18] and Miner and Lewis[19] and use the reaction-rate data of Bortner.[20] Reaction 8 of Table 1 is based on the wake studies of Cresswell et al.[21] The next 13 carbon-related reactions (9–21) are based on the work of Blottner,[22] and the subsequent 14 fluorocarbon reactions (22–35) are based on the work of Cresswell et al.[21] and Braun.[23] The last fluorocarbon reaction is based on the work of Modica.[24] The equilibrium constants (K_c) for these reactions were calculated using curvefits of species partition functions collected by Modica.[24]

Table 1 Forward reaction rate data

$K_{fr} = C0_r^*(T^{**}C2_r)^*\exp(-C1_r/T)$							T, K		
	Reaction						$C0_r$	$C1_r$	$C2_r$
(1)	O2	+M1	=2O	+M1			3.61E+18	59400.0	−1.00
(2)	N2	+M2	=2N	+M2			1.92E+17	113100.0	−0.50
(3)	N2	+N	=2N	+N			4.15E+22	113100.0	−1.50
(4)	NO	+M3	=N	+O	+M3		3.97E+20	75600.0	−1.50
(5)	O	+NO	=N	+O2			3.18E+09	19700.0	1.00
(6)	O	+N2	=N	+NO			6.75E+13	37500.0	0.00
(7)	O	+N	=NO+	+e−			9.03E+09	32400.0	0.50
(8)	N2	+O2	=2NO				6.69E+09	64638.7	−2.54
(9)	CO2	+M4	=CO	+O	+M4		1.20E+11	36850.0	0.50
(10)	CO	+M5	=C	+O	+M5		8.50E+19	129000.0	−1.00
(11)	Na	+O2	=Na+	+O2−			1.07E+17	54105.1	0.07
(12)	Na	+O	=Na+	+O−			1.46E+19	42189.7	−0.70
(13)	Na	+M6	=Na+	+e−	+M6		1.62E+12	59187.5	1.46
(14)	Na	+e−	=Na+	+e−	+e−		2.16E+31	59187.5	−3.04
(15)	O−	+M7	=O	+e−	+M7		1.48E+11	16997.8	1.05
(16)	O2−	+M7	=O2	+e−	+M7		1.87E+10	5082.4	0.90
(17)	C2F4	+M6	=2CF2	+M6			4.08E+40	37695.0	−6.36
(18)	C2F4	+O	=COF2	+CF2			1.33E+08	215.0	−1.55
(19)	CF2	+O2	=CO	+2F	+O		2.92E+10	6682.6	0.50
(20)	CF4	+M6	=CF2	+2F	+M6		9.24E+14	48130.6	0.50
(21)	COF2	+M6	=CO	+2F	+M6		4.29E+11	27965.8	0.50
(22)	F2	+M6	=2F	+M6			7.90E+12	18474.7	0.20
(23)	F2	+e−	=F	+F−			3.30E+15	0.0	0.00
(24)	F−	+M6	=F	+e−	+M6		3.00E+11	40015.4	0.70
(25)	C2	+M8	=2C	+M8			4.50E+18	70930.0	−1.00
(26)	C3	+M9	=C	+C2	+M9		1.60E+16	87480.0	1.00
(27)	2CO	=C2	+O2				9.20E+11	163300.0	0.75
(28)	CO	+C	=C2	+O			4.10E+10	59790.0	0.50
(29)	C2	+CO	=C3	+O			1.20E+13	43240.0	0.00
(30)	C3	+C	=C2	+C2			1.70E+09	19580.0	1.50
(31)	CO	+NO	=CO2	+N			1.00E+03	20980.00	2.00
(32)	CO2	+O	=CO	+O2			3.00E+08	18210.00	1.00
(33)	CO	+CO	=CO2	+C			1.00E+03	72390.00	2.00
(34)	CO	+O	=O2	+C			2.00E+10	69500.00	1.00
(35)	CO	+N	=NO	+C			9.00E+16	53200.00	−1.00
(36)	CF2	+O2	=COF2	+O			4.80E−14	6640.00	0.50

For the present nonequilibrium calculations, the thermodynamic properties (enthalpy and specific-heat data) of the air species (O, O_2, NO, NO^+, N, and N_2) were obtained from the thermodynamic data of Browne.[25–27] For the 23-species Teflon-air chemical system, the thermodynamic properties for the carbon species (C, C_2, C_3, CO, and CO_2) were obtained from Blottner et al.[18] The thermodynamic data for the remaining species (Na, Na^+, O^-, O_2^-, CF_2, CF_4, F, F_2, F^-, C_2F_4, and COF_2) are based on the data used by Bhutta and Lewis.[5]

The viscosity data for O, O_2, NO, NO^+, N, N_2, C, C_2, C_3, CO, and CO_2 are based on the data used by Blottner et al.[18] The viscosity data for the remaining species (Na, Na^+, O^-, O_2^-, CF_2, CF_4, F, F_2, F^-, C_2F_4, and COF_2) are based on the data used by Bhutta and Lewis[5] and Bhutta et al.[6] The thermal conductivity of the individual species is calculated from the Eucken semiempirical formula, and the viscosity and thermal conductivity of the mixture are calculated using Wilke's semiempirical relations.

Table 2 Thermal conductivity curvefits for air species

Species	A_i[a]	B_i[a]	C_i[a]
N2	−0.33734053E−01	0.12824953E+01	−0.29808637E+01
O2	−0.46498024E−01	0.14800828E+01	−0.36461138E+01
NO	−0.34769636E−01	0.13217918E+01	−0.31735793E+01
O	0.13789297E−01	0.51425073E+00	0.53814451E+00
N	−0.89982103E−03	0.79150022E+00	−0.85718251E+00
NO+	−0.28978117E+00	0.82323298E+01	−0.50167470E+02

[a] $\ell n\ [k_i(mW/m-K)] = C_i + (A_i\ \ell n T + B_i)\ \ell n\ T$ where T is the temperature in Kelvin.

The diffusion model used in the present study was limited to binary diffusion. For the Teflon-air calculations, the binary diffusion coefficients were specified using a constant binary Lewis number of 1.4. However, for the clean-air (O, N, NO, NO^+, O_2, and N_2) calculations, we also used Blottner et al.'s curvefits of the binary diffusion coefficients[18] to investigate the effects of variable binary Lewis number. Furthermore, in the case of clean-air calculations, we also studied the impact of the Eucken approximation for the species thermal conductivity. To improve these data, we curvefit the thermal conductivity calculations of Uribe et al.[28] for N_2, O_2, and NO and the calculations of Biolsi[29] for N, O, and NO^+ with a quadratic least-square fit in the log-log plane. The resulting curvefits (Table 2) represent the respective data of Uribe et al.[28] and Biolsi[29] to an accuracy of ±2%.

Solution Scheme

The coordinate system used for the present axisymmetric afterbody PNS scheme is a general curvilinear coordinate system (ξ_1, ξ_2, ξ_3). The ξ_1 coordinate is along the body and is also the marching direction, the axis-normal ξ_2 coordinate stretches from the body to the outer bow shock, and the ξ_3 coordinate is the circumferential coordinate measured from the windward pitch plane to the leeward pitch plane. Also, a body-fixed orthogonal (Cartesian) coordinate system is chosen such that the origin of the Cartesian coordinate system is at the tip of the blunt nose, and the x axis is aligned with the axis of the body. It should be noted that, although the ξ_3 coordinate appears in this discussion, the final formulation uses the axisymmetric nature of the flow to do the exact crossflow derivatives along the windward ($\xi_3 = 0$) streamline.

Governing Equations

We choose our vector of flowfield unknowns to be

$$q = [\rho,\ \rho u,\ \rho w,\ \rho T,\ p]^T \tag{1}$$

Following the approach of Viviand[30] and Peyert and Viviand,[31] the three-dimensional Navier-Stokes equations are transformed into the general curvilinear coordinate system (ξ_j). These three-dimensional Navier-Stokes equations are elliptic in ξ_1, ξ_2, and ξ_3 directions. After neglecting the viscous dissipation effects in the ξ_1 direction and making use of the axisymmetric nature of the flowfield, we obtain the following vectorial form of the axisymmetric PNS equations:

$$f_{1,\xi_1} + f_{2,\xi_2} - \epsilon s_{2,\xi_2} = h \tag{2a}$$

where $\epsilon = M_\infty/Re_\infty$, and it is assumed that the freestream behaves like a perfect gas.

These five equations representing the differential conservation of mass, momentum, and energy are mathematically closed by using the equation of state for the particular gas model being used. In the case of finite-rate chemically reacting air, the gas is assumed to be a mixture of perfect gases and the equation of state is given by

$$p - \rho T/\bar{m} = 0 \tag{2b}$$

where $\bar{m} = \gamma_\infty \bar{m}^*/\bar{m}^*_\infty$ is the nondimensional mixture molecular weight. It should be noted that, unlike our previous nonequilibrium PNS calculations,[1-6] the energy equation for the present study is written in terms of the conservation of total enthalpy.

The mixture thermodynamic properties (such as $\bar{m}$, $\bar{k}$, $\overline{C_p}$, $\bar{\mu}$, Pr, etc.) require a knowledge of the species concentrations (C_i) that is obtained from the species conservation equations.[32] These equations are first transformed into the (ξ_1, ξ_2, ξ_3) coordinate system, and the resulting equations are parabolized by neglecting diffusion effects in the ξ_1 direction. Furthermore, for axisymmetric flows there are no crossflow (ξ_3) species convection and dissipation effects ($C_{i,\xi_3} = C_{i,\xi_3\xi_3} = 0$). The final axisymmetric parabolized species conservation equations are written as

$$[(\rho U_1/J)C_i]_{,\xi_1} + [(\rho U_2/J)C_i]_{,\xi_2} - \epsilon[(\bar{\mu} Le_i m_{2kk}/JPr)C_{i,\xi_2}]_{,\xi_2} = \dot{\omega}_i \tag{3}$$

where $i = 1, 2, 3, \ldots, NS$.

Numerical Solution Scheme

The system of equations represented by Eqs. (2) and (3) is closed through a knowledge of the thermodynamic and transport properties of the mixture; namely, $\overline{C_p}$, $\bar{k}$, $\bar{m}$, $\bar{\mu}$, Pr, and Le. The overall nonequilibrium PNS problem represented by these equations is well posed; however, the number of unknowns involved is very large (i.e., ρ, ρu, ρv, ρw, ρT, p, $\overline{C_p}$, $\bar{k}$, $\bar{m}$, $\bar{\mu}$, Pr, C_1, C_2, C_3, . . . , C_{NS}). However, for many practical problems, the coupling between the fluid mechanics (ρ, ρu, ρv, ρw, ρT, and p) and the chemistry ($\overline{C_p}$, $\bar{m}$, $\bar{k}$, $\bar{\mu}$, Pr, C_1, C_2, . . . , C_{NS}) is not very strong, and we can decouple the overall nonequilibrium PNS problem into 1) a fluid mechanics problem and 2) a chemistry problem.[1-6] During each iteration at a given marching step, we first solve the fluid mechanics problem [Eqs. (2a-2b)], and then we solve the chemistry problem [Eq. (3)] based on the solution to the fluid mechanics problem. With this updated chemistry, the fluid mechanics problem is solved once again, and the cycle is repeated until acceptable convergence is achieved.

1) Solution of the Fluid Mechanics Problem

The solution scheme used for the fluid mechanics problem is very similar to our approach of Refs. 1-6 and 12. However, briefly speaking, it is assumed that the solution at the "$n+1$"

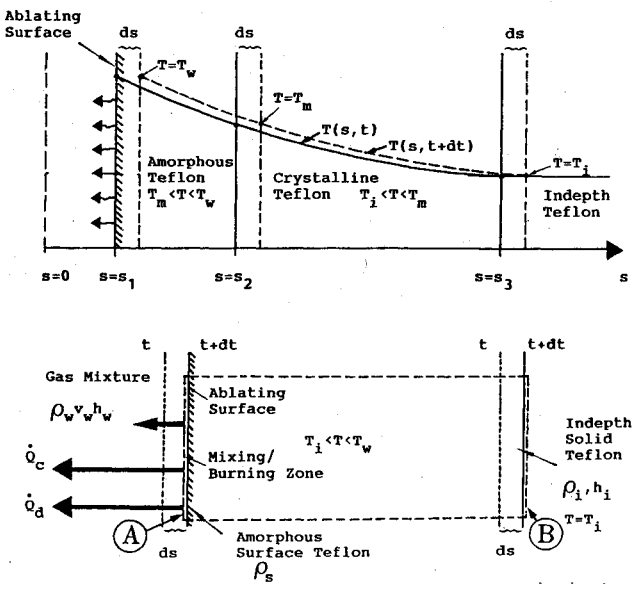

Fig. 1 Schematic description of quasisteady surface ablation and energy balance.

level is close to the solution at the nth iteration. By expanding the solution around the nth iteration, using two-point streamwise differencing, and fourth-order axis-normal numerical diffusion effects,[12] we can write Eqs. (2a–2b) as

$$\left(\frac{A_1}{\Delta\xi_1} - A_0\right)^n \cdot \Delta\chi^{n+1} + [(A_2^n - \epsilon M_2^n) \cdot \Delta\chi^{n+1}]_{,\xi_2} = -\omega[f_{1,\xi_1} + f_{2,\xi_2} - \epsilon s_{2,\xi_2} - h]^{j+1,n} \tag{4a}$$

where the intermediate (unsmooth) solution vector[12] ($\chi^{j+1,n+1}$) is given by

$$\Delta\chi^{n+1} = \chi^{j+1,n+1} - \chi^{j+1,n} \tag{4b}$$

After the iterative process of Eqs. (4a) and (4b) converges, the final (smooth) solution vector[12] (q^{j+1}) is obtained from

$$q^{j+1} = \chi^{j+1} - [0, 0, 0, 0, (\chi_6)_{,\xi_2\xi_2\xi_2\xi_2}]^T \Delta\xi_2^4/16 \tag{4c}$$

The matrices A_0, A_1, A_2, and M_2 are called the Jacobian matrices,[5,12] ω is an under-relaxation factor that has values between 0 and 1,[12] and χ_6 is the sixth element of the vector χ.

Since the fourth-order axis-normal dissipation effects introduced through Eq. (4c) act only on the pressure field, they do not degrade the wall heat-transfer and skin-friction predictions.[12] Furthermore, to damp and control the growth of any streamwise numerical oscillations, small amounts of second-order streamwise numerical dissipation effects are also added to the governing equations.[12] Based on a simple damping model, we choose the streamwise diffusion effects to be of the form[12]

$$f_{1,\xi_1} \cong (f_{1,\xi_1})_b - \omega f_{1,\xi_1\xi_1}\Delta\xi_1 \tag{5}$$

where the subscript b represents first-order backward-differenced approximation. The appropriate values of ω are between 0 and 1, and its form is chosen such that $\omega \to 1$ as $\Delta\xi_1 \to 0$ and $\omega \to 0$ when $\Delta\xi_1$ is sufficiently large. Thus, the numerical accuracy of a large step-size solution is not compromised.

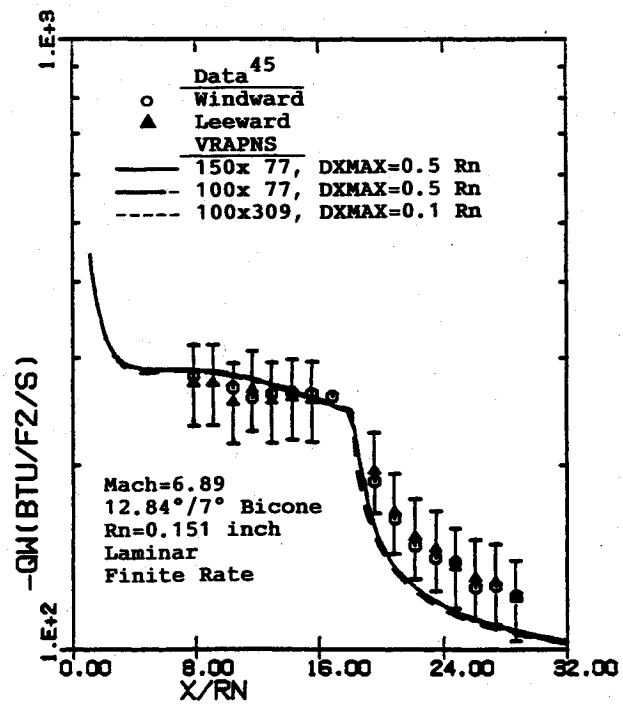

Fig. 2 Grid-refinement effects on the predictions of wall heat-transfer rate for case 1.

2) Solution of the Chemistry Problem

Using the solution of the fluid mechanics problem [Eqs. (2) and (4)], first the thermodynamic and transport properties of the reacting gas mixture are determined. This information is then used to solve the coupled species equations that assume that in all there are *NE* elements and *NS* total species. The *NS*th species is always chosen to be the electrons, which have negligible mass, and, thus, $C_{e^-} = 0$. Although there are *NS* species, only $NS - 1$ species mass fractions need to be determined. In general, the $NS - 1$ species are split into two user-specified groups of *NM* and *NE* species, where $NM + NE = NS - 1$. For simplicity, let us refer to the group containing the *NE* species as group 1 and the group containing *NM* species as group 2. The purpose is to try to include in group 1 not only the most dominant species but also to select these *NE* species such that all available elements are represented. The remaining *NM* species are left in the other group (group 2). The reason behind this grouping is to obtain the *NM* number of relatively less dominant species from the corresponding species conservation equations (second-order partial differential equations), whereas the concentrations of the dominant species are determined from the *NE* number of algebraic relations representing the conservation of elemental mass. In this manner the final species concentration distributions are better behaved and are less prone to numerical errors and oscillations.

In general the coupled-species solution for the chemistry problem consists of the following main steps:

1) Obtain the element mass fractions (E_e) of all elements at each grid point using the element conservation equations.

2) Set up *NE* algebraic equations representing the conservation of elemental mass at each grid point.

3) Set up *NM* differential equations representing the conservation of mass of the *NM* species included in group 2.

4) Solve the $NE + NM$ equations simultaneously to obtain the species mass fractions at each grid point.

These steps are discussed in the following sections in more detail.

Solution of the Element Conservation Equations

The parabolized axisymmetric element conservation equations are almost identical in form to the species conservation equation [Eq. (3)], except that they do not contain any production terms. These parabolized element conservation equations can be written as

$$[(\rho U_1/J)E_e]_{,\xi_1} + [(\rho U_2/J)E_e]_{,\xi_2} - \epsilon[(\tilde{\mu}Lem_{2kk}/JPr)E_{e,\xi_2}]_{,\xi_2} = 0 \tag{6}$$

where $e = 1, 2, 3, \ldots, NE$. It should be noted that these equations are mutually uncoupled and numerically the most effective way of solving these element conservation equations is to solve for all but the most dominant element species from the $NE - 1$ element conservation equations, and the element mass fraction of the last (*NE*th) element is then obtained from the constraint

$$\sum_{e=1}^{NE} E_e = 1$$

The boundary conditions for the element conservation equations [Eq. (6)] consist of specified element mass fractions at the shock [$(E_e)_{\text{shock}} = (E_e)_\infty$]. The wall boundary conditions for these elemental conservation equations are, however, slightly more complicated. In the case of a nonablating wall, the elemental composition at the wall is simply $(E_e)_w = (E_e)_\infty$. However, in the case of an ablating wall, the wall boundary conditions consist of convection of elements away from the wall and diffusion of elements toward the wall. This convection-diffusion boundary condition is in fact a first-order differential equation written as

$$(\rho U_2/J)E_e - \epsilon(\tilde{\mu}Lem_{2kk}/JPr)E_{e,\xi_2} = \dot{m}(\xi_{2,z}/J)(E_e)^- \tag{7}$$

where $(E_e)^-$ is the elemental mass fraction of the injectant, and $\dot{m}$ is the surface ablation rate.

Element Mass Constraints

Once the element conservation equations have been solved to give the element mass fractions at each grid point, the local species must satisfy the *NE* number of constraints defining the conservation of atomic mass. The constraint conditions are algebraic relations that imply that at any grid point the number of atoms of element *e* in all species must add up to its local value dictated by the element conservation equations.

In terms of mass fractions, these constraint conditions can be written as

$$\sum_{i=1}^{NE}\left[\frac{(\alpha_e)_i A_e}{M_i}\right] C_i = E_e \tag{8}$$

where $(\alpha_e)_i$ is the number of atoms of element *e* in species *i*, A_e is the atomic weight of element *e*, and M_i is the molecular weight of species *i*.

Suppose we define the vector of element mass fractions as $\boldsymbol{e}$, the vector of species mass fractions for group 1 species as $\boldsymbol{c}_1$, and the vector of species mass fractions for group 2 species as $\boldsymbol{c}_2$; then

$$\begin{aligned} \boldsymbol{e} &= [E_1, E_2, \ldots, E_{NE}]^T \\ \boldsymbol{c}_1 &= [C_{1-1}, C_{1-2}, \ldots, C_{1-NE}]^T \\ \boldsymbol{c}_2 &= [C_{2-1}, C_{2-2}, \ldots, C_{2-NM}]^T \end{aligned} \tag{9}$$

where $C_{1-1}, C_{1-2}, \ldots, C_{1-NE}$ are the *NE* number of species in group 1, and $C_{2-1}, C_{2-2}, \ldots, C_{2-NM}$ are the *NM* number of species in group 2.

Using this notation, we can rewrite the element mass constraints of Eq. (8) as

$$\sum_{j=1}^{NE}\left[\frac{(\alpha_e)_{i-j} A_e}{M_{1-j}}\right] C_{1-j} + \sum_{k=1}^{NM}\left[\frac{(\alpha_e)_{2-k} A_e}{M_{2-k}}\right] C_{2-k} = E_e \tag{10}$$

This is a vectorial equation that can be written at the $n+1$ iteration as

$$[\boldsymbol{a}_1(\boldsymbol{c}_1)^{n+1}] + [\boldsymbol{a}_2(\boldsymbol{c}_2)^{n+1}] = \boldsymbol{e}^{n+1} \tag{11}$$

The changes in species mass fractions $(\Delta C_{1-j}, \Delta C_{2-k})$ are numerically not the most desirable variables to solve for because during the iterations the solution changes can be negative and, thus, the mass fractions of trace species can temporarily become negative. This would not only be a nonphysical situation but also, more importantly, it can cause fatal computational errors. To avoid such computational difficulties, the dependent variables are transformed from species mass fractions (C_i) to the log of moles of these species per unit volume (L_i), where

$$L_i = \ell n\,[\rho C_i / M_i] \tag{12}$$

and $i = 1, 2, 3, \ldots, NS$. Thus, we can linearize Eq. (11) around the previous iteration, and using vector notation we can write them as

$$\boldsymbol{W}_{11}^n \cdot \Delta \boldsymbol{l}_1 + \boldsymbol{W}_{12}^n \cdot \Delta \boldsymbol{l}_2 = -[\boldsymbol{a}_1 + \boldsymbol{a}_2 - \boldsymbol{e}]^n = \boldsymbol{d}_1^n \tag{13}$$

Using Eq. (13), we can now express $\Delta \boldsymbol{l}_1$ in terms of $\Delta \boldsymbol{l}_2$ as

$$\Delta \boldsymbol{l}_1 = -[\boldsymbol{W}_{11}^{-1}]^n \cdot \boldsymbol{W}_{12}^n \cdot \Delta \boldsymbol{l}_2 + [\boldsymbol{W}_{11}^{-1}]^n \cdot \boldsymbol{d}_1^n = -\boldsymbol{B}_1 \cdot \Delta \boldsymbol{l}_2 + \boldsymbol{b}_1 \tag{14}$$

Solution of the Species Conservation Equations

For the *NM* species $(\boldsymbol{c}_2)$ in group 2, we can also rewrite the species conservation equation [Eq. (3)] in the following vectorial form:

$$[(\rho U_1/J)\boldsymbol{c}_2]_{,\xi_1} + [(\rho U_2/J)\boldsymbol{c}_2]_{,\xi_2} - \epsilon[(\bar{\mu} Lem_{2kk}/JPr)\boldsymbol{c}_{2,\xi_2}]_{,\xi_2} = \dot{\omega}(\boldsymbol{c}_1, \boldsymbol{c}_2) \tag{15}$$

where $\dot{\omega}$ is a vector containing the production terms for the group 2 species $(\boldsymbol{c}_2)$. These species production terms can be linearized around the previous iteration as

$$\begin{aligned} \dot{\omega}^{n+1} - \dot{\omega}^n &\cong (\partial\dot{\omega}/\partial l_1)^n \Delta \boldsymbol{l}_1 + (\partial\dot{\omega}/\partial l_2)^n \Delta \boldsymbol{l}_2 \\ &= \boldsymbol{W}_{21}^n \cdot \Delta \boldsymbol{l}_1 + \boldsymbol{W}_{22}^n \cdot \Delta \boldsymbol{l}_2 \end{aligned} \tag{16}$$

Thus, using Eq. (16) we can write the species production terms in terms of only $\Delta \boldsymbol{l}_2$ as

$$\begin{aligned} \dot{\omega}^{n+1} - \dot{\omega}^n &\cong [\boldsymbol{W}_{22}^n - \boldsymbol{W}_{21}^n \cdot \boldsymbol{B}_1] \cdot \Delta \boldsymbol{l}_2 + \boldsymbol{W}_{21}^n \cdot \boldsymbol{b}_1 \\ &= \boldsymbol{B}_2 \cdot \Delta \boldsymbol{l}_2 + \boldsymbol{b}_2 \end{aligned} \tag{17}$$

Now, using Eq. (17) we can linearize each component of the species conservation equation [Eq. (15)] around the previous iteration. Using two-point backward-differenced approximation for the streamwise derivative, we can write

$$[(\rho U_1/J)\boldsymbol{c}_2]_{,\xi_1}^{n+1} \cong [(\rho U_1/J)\boldsymbol{c}_2]_{,\xi_1}^n + \frac{1}{\Delta\xi_1} \boldsymbol{D}_1^n \cdot \Delta \boldsymbol{l}_2 \tag{18a}$$

Similarly, we can write

$$[(\rho U_2/J)\boldsymbol{c}_2]_{,\xi_2}^{n+1} \cong [(\rho U_2/J)\boldsymbol{c}_2]_{,\xi_2}^n + [\boldsymbol{D}_2^n \cdot \Delta \boldsymbol{l}_2]_{,\xi_2} \tag{18b}$$

and

$$\epsilon[(\bar{\mu} Lem_{2kk}/JPr)\boldsymbol{c}_{2,\xi_2}]_{,\xi_2}^{n+1} \cong \epsilon[(\bar{\mu} Lem_{2kk}/JPr)\boldsymbol{c}_{2,\xi_2}]_{,\xi_2}^n + \epsilon[\boldsymbol{D}_3^n \cdot \Delta \boldsymbol{l}_2]_{,\xi_2} \tag{18c}$$

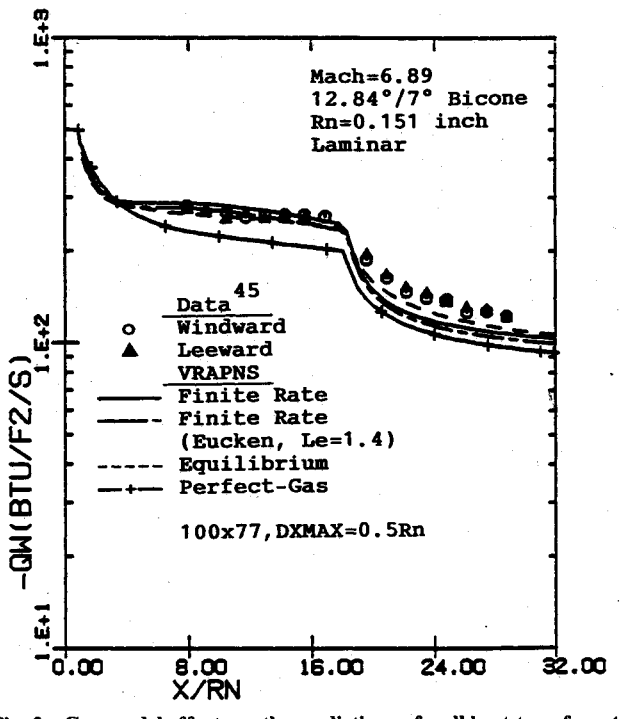

Fig. 3 Gas-model effects on the predictions of wall heat-transfer rate for case 1.

Using Eqs. (17) and (18), we can write the species conservation equations for the group 2 species [Eq. (15)] in the following block-matrix form

$$[(1/\Delta\xi_1)\boldsymbol{D}_1 + \boldsymbol{B}_2]^n \cdot \Delta\boldsymbol{l}_2 + [\boldsymbol{D}_2^n \cdot \Delta\boldsymbol{l}_2]_{,\xi_2} - \epsilon[\boldsymbol{D}_3^n \cdot \Delta\boldsymbol{l}_2]_{,\xi_2}$$
$$= -\{[(\rho U_1/J)\boldsymbol{c}_2]_{,\xi_1} + [(\rho U_2/J)\boldsymbol{c}_2]_{,\xi_2}$$
$$-\epsilon[(\bar{\mu}Lem_{2kk}/JPr)\boldsymbol{c}_{2,\xi_2}]_{,\xi_2} - \dot{\omega} - \boldsymbol{b}_2\}^n = \boldsymbol{b}^n \qquad (19)$$

Equation (19) represents a block tridiagonal system of equations in the ξ_2 direction. It should be noted that in Eq. (19) all of the matrices except the the matrix $\boldsymbol{B}_2$ are diagonal in form, and the mutual coupling of the species equations is solely due to this matrix. This block-matrix system of equations can now be solved using the following solution approaches involving various levels of approximations about the nature of solution coupling between the various species.

1) Diagonalized Solution Scheme

This solution scheme assumes that the local production of a particular species is dominated by the local concentration of that species. This is typically a good approximation under nonequilibrium flow conditions and is a very poor approximation under equilibrium or near-equilibrium flow conditions. For this scheme, all off-diagonal terms of the matrix $\boldsymbol{B}_2$ in Eq. (17) are neglected, and thus all matrices in Eq. (19) become diagonal. Consequently, each equation represented by Eq. (19) can now be solved uncoupled from all others using a simple scalar tridiagonal solver. Except for the exact form of the dependence of the production term of a particular species on the local concentration of that species [Eq. (17)], this approach is very similar to the classical uncoupled solution approach (Blottner,[22] Davis,[33] Moss,[34] Miner and Lewis,[19] Bhutta and Lewis,[1-5] and Bhutta et al.[2,6]) and, thus, will suffer from similar stiffness problems under equilibrium and near-equilibrium conditions.

2) Strongly Implicit Solution Scheme

This solution approach assumes that the local production of each species can be affected by all species involved in reacting with that species and, thus, retains the complete full-matrix form of matrix $\boldsymbol{B}_2$ in Eq. (17). Thus, by using two-point backward-differenced approximations for the ξ_1 derivatives, central-differenced approximations for the ξ_2 and ξ_3 derivatives, and using ℓ as the grid index in the ξ_2 direction, we can write Eq. (19) as

$$\boldsymbol{A}_\ell \cdot (\Delta\boldsymbol{l}_2)_{\ell-1} + \boldsymbol{B}_\ell \cdot (\Delta\boldsymbol{l}_2)_\ell + \boldsymbol{C}_\ell \cdot (\Delta\boldsymbol{l}_2)_{\ell+1} = \boldsymbol{d}_\ell \qquad (20)$$

This block-tridiagonal system of equations can now be solved using the appropriate species boundary conditions at the wall ($\ell = 1$) and at the shock ($\ell = LMAX$). This block-matrix solution approach properly accounts for the mutual coupling of all species and, thus, avoids the problems of numerical stiffness.

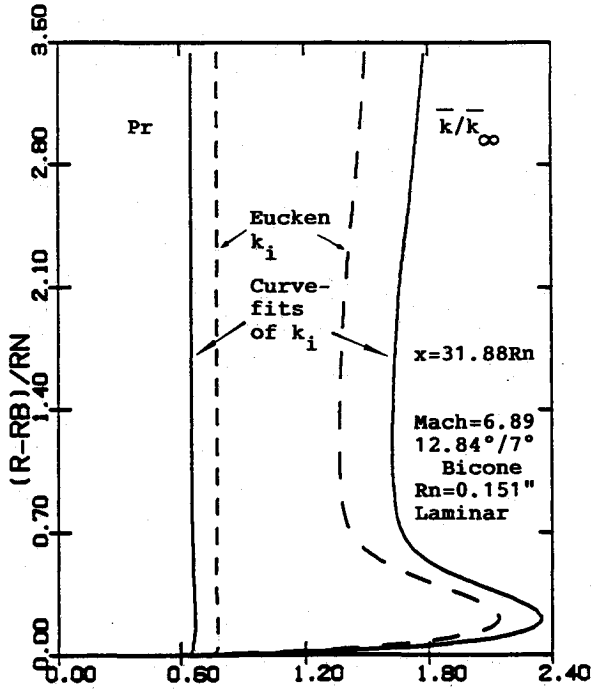

Fig. 4 Effects of thermal conductivity data on mixture properties at the body end for case 1.

3) Two-Step Solution Scheme

This solution approach is a very attractive compromise between the coupling characteristics of the block-matrix solution scheme (2) and the efficiency characteristics of the diagonalized (uncoupled) solution scheme (1). In this approach, it is assumed that 1) the spatial coupling of a species at a grid point is predominantly dictated by only the concentration of that species at the neighboring grid points and 2) the mutual coupling of the species at a grid point is predominantly dictated by the species concentrations at that grid point. Thus we devise a two-step procedure in which the first solution step accounts for the spatial coupling of each species, and the second step accounts for the local mutual coupling of the species. The first step in this two-step procedure consists of a diagonalized solution scheme, and the resulting solution is called an intermediate solution. Using this intermediate solution in Eq. (19), the off-diagonal terms (representing the spatial coupling effects) are estimated, and the resulting system of equations is reduced to a simple point-matrix solution. Furthermore, this procedure is highly vectorizable because the matrix inversion at each grid point can be done in a single vector loop over all grid points. Numerical experience shows that this additional matrix inversion only takes approximately 15% more time than the diagonalized scheme; however, since it retains the mutual coupling of the species at a grid point [Eq. (17)], it also avoids the numerical stiffness problems under equilibrium and near-equilibrium flow conditions. It is worth noting that under the nonequilibrium limit the first step of this two-step procedure is dominant and sufficient, whereas in the equilibrium limit the second step of this two-step procedure is dominant and represents a point-by-point application of the law of mass action.

The final system of equations representing the species conservation equations can now be solved using the appropriate species boundary conditions at the wall ($\ell = 1$) and at the shock ($\ell = LMAX$). Once the $\Delta\boldsymbol{l}_2$ vector has been obtained at all of the grid points, the corresponding $\Delta\boldsymbol{l}_1$ vector is readily obtained using Eq. (14). The important thing to note in this solution is that, unlike a full matrix solution of the species conservation equations that involves inverting and iterating on matrices of $NS \times NS$ size, the present solution scheme operates and iterates on matrices that are primarily $NM \times NM$ in size. This smaller size of the matrices is not only computationally more efficient, but also the overall iterative process is much faster to converge.

Although the iterations are done in terms of the logarithm of the molar concentrations, the actual computations are still done in terms of the species mass fractions (c_1, c_2). Thus, after each iteration a decoding procedure is required to convert the changes in the log of the molar concentrations to the corresponding changes in the mass fractions. It is also important to note that, although the logarithm of the molar concentration is a better variable to iterate on because of its nonnegative character, due to its exponential nature, sometimes during the iterations it can attain unrealistically large values. The follow-

ing decoding strategy helps circumvent these problems of nonnegativity as well as exponential growth:

$$\Delta C_i^{n+1} = \begin{cases} C_i^n[\exp(\Delta L_i^{n+1}) - 1] & \text{if } \Delta L_i^{n+1} \le 0 \\ C_i^n \Delta L_i^{n+1} & \text{if } \Delta L_i^{n+1} > 0 \end{cases} \quad (21)$$

where $i = 1, 2, \ldots, NS$.

Additional Numerical Considerations

In this study we have used our fully implicit shock-fitting scheme[3-6,12] that was modified to treat frozen as well as equilibrium shock-crossing conditions. In this scheme the bow shock location is iteratively predicted as the solution marches down the body. This shock-fitting scheme uses a general curvilinear coordinate system and can treat various gas models (perfect gas or equilibrium air or nonequilibrium air) accurately and in a unified manner.

Furthermore, it should be noted that the terms on the right-hand side of Eq. (4a) are the governing differential equation corresponding to the fluid mechanics problem written at the nth iteration level and goes to zero in the limit of convergence. Under these near-convergence conditions, the exact form of the left-hand implicit terms is not very important because it only affects the convergence path of the solution.[1-12] Consequently, we do not update the Jacobian matrices beyond the first iteration. With this (pseudo-unsteady) approach, the time for each iteration after the first iteration ($n = 2, 3, \ldots$) is only 10% of the time taken by the first iteration.

The problem represented by the governing axisymmetric PNS equations is a split-boundary-value problem; i.e., the equations are hyperbolic parabolic in the ξ_1 direction and elliptic in the ξ_2 direction. Thus, to solve the problem completely, we need initial conditions to be specified at the start of the marching procedure and boundary conditions to be specified at the wall and at the outer bow shock. The initial conditions to start the present axisymmetric PNS scheme were obtained from compatible axisymmetric blunt-body viscous shock-layer (VSL) schemes,[35,36] and the shock boundary conditions were imposed using the implicit shock-fitting approach mentioned earlier.

The flowfield boundary conditions at the wall consist of 1) equation of state of the gas [$p - \rho T/\bar{m} = 0$], 2) no-slip condition for u velocity component [$\rho u = 0$], 3) specified surface ablation rate [$\rho w = \dot{m}$], 4) specified wall temperature [$(\rho T) = \rho T_w$], and 5) zero pressure derivative in the ξ_2 direction [$p_{,\xi_2} = 0$]. The corresponding wall boundary conditions for the coupled-species conservation equations [Eq. (3)] consist of either 1) a fully catalytic wall [$C_i = C_{i\infty}$], or 2) an equilibrium-catalytic wall [$C_i = C_i^{EQ}(\rho_w, T_w)$], where $i = 1, 2, \ldots, NS$.

New Quasisteady Ablation Model for Teflon

Teflon (DuPont trade name) is a tetrafluoroethylene polymer that is widely used as a low-temperature ablator for re-entry applications. This section provides a brief description of a completely quasisteady surface ablation model for Teflon. This model only requires the assumption of quasisteady conditions and accounts for the different densities of Teflon in crystalline and amorphous states. The various aspects of this surface ablation model are described in the following sections.

Quasisteady Assumption

The assumption of quasisteady conditions implies that the temperature distribution inside the material relative to the moving surface does not change with time. This is schematically shown in Fig. 1, where the coordinate s is directed into the material and $s = s_1(t)$ is the amount of surface recession at any given time t. This quasisteady assumption means that during a differential time interval dt, the surface at $s = s_1(t)$, the amorphous-crystalline interface at $s = s_2(t)$, and the in-depth material interface at $s = s_3(t)$ move by the same differential increment ds (see Fig. 1). Furthermore, the quasisteady assumption also implies that the surface as well as all of the other material interfaces move at a constant rate; i.e., $\dot{s} = ds/dt = ds_1/dt = ds_2/dt = ds_3/dt = \text{const}$.

Variable Material Density

As shown in Fig. 1, the temperature within the ablating Teflon layer varies with depth. The three distinct regions of this temperature distribution are 1) in-depth solid Teflon with $T = T_i$, 2) solid (crystalline) Teflon layer with $T_i < T \le T_m$, and 3) amorphous (gel) Teflon layer with $T_m < T \le T_w$ (where T_i is the in-depth temperature, T_m is Teflon's melting temperature, and T_w is the wall temperature). The density of surface (amorphous) Teflon is quite different from the density of in-depth (crystalline) Teflon, and if we denote the density of the surface material by ρ_s and that of the in-depth material by ρ_i, then based on the work of Holzknecht[37] and Arai[38] we can express these densities as

$$\rho_s = 2.07 - 7.00 \times 10^{-4} T_w \quad (\text{g/cm}^3)$$
$$\rho_i = 2.119 + 7.92 \times 10^{-4} T_i - 2.105 \times 10^{-6} T_i^2 \quad (\text{g/cm}^3) \quad (22)$$

where T_w and T_i are in Kelvin.

Conservation of Mass at the Ablating Surface

Let us denote the density of the gaseous mixture at the wall (after mixing and burning) by ρ_w and the gas-phase convection velocity by v_w. If ds/dt is the surface recession rate and ρ_s is the surface material density given by Eq. (32), then the conservation of mass at the surface gives the surface ablation rate ($\dot{m}$) as

$$\dot{m} = \rho_w v_w = \rho_s \frac{ds}{dt} \quad (23)$$

Surface Energy Balance

With the quasisteady ablation model, relative to the moving surface, things do not change with time. Thus, at any time we can draw a control volume such that it moves along with the receding surface and includes the entire ablating surface layer. Briefly speaking, the lower surface of this control volume

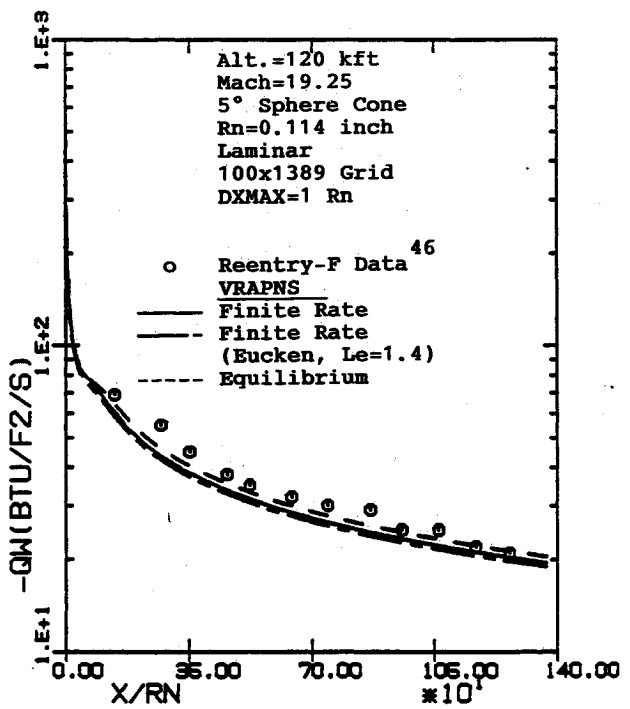

Fig. 5 Comparison of predicted wall heat-transfer rate for case 2.

(denoted by B) is aligned with the start of the in-depth material with density ρ_i and specific enthalpy h_i. The upper surface of this control volume (denoted by A) is aligned with the gas-phase interface that is adjacent to the receding surface. The mixing and burning of the Teflon monomer with air is assumed to occur in the infinitesimally thin layer between the surface and the gas-phase interface adjacent to it. It should be noted that the lower surface (B) of this control volume is taken sufficiently in-depth such that at any instant at this surface $T = T_i$ and $\partial T/\partial s = 0$. Thus, there is no conduction heat loss across the lower surface (B) of the moving control volume.

The energy balance across the control volume gives

$$\begin{array}{c}\text{Rate of energy leaving surface } A \\ \dot{Q}_c \quad + \quad \dot{Q}_d \quad + \quad \rho_w v_w h_w \\ \text{(convection)} \quad \text{(diffusion)} \quad \text{(mass transfer)}\end{array} = \begin{array}{c}\text{Rate of energy entering surface } B \\ \rho_i \dfrac{ds}{dt} h_i \\ \text{(in-depth material)}\end{array} \tag{24}$$

where h_w is the specific enthalpy of the gaseous mixture at the wall and h_i is the specific enthalpy of the in-depth solid Teflon.

Using Eq. (23), we can write Eq. (24) as

$$\dot{Q}_c + \dot{Q}_d + \dot{m} h_w = \dot{m}\left(\frac{\rho_i}{\rho_s}\right) h_i \tag{25}$$

Thus, the quasisteady surface ablation rate ($\dot{m}$) for Teflon becomes

$$\dot{m} = \frac{-[\dot{Q}_c + \dot{Q}_d]}{[h_w - (\rho_i/\rho_s) h_i]} \tag{26}$$

All of the quantities on the right-hand side of this expression are either directly known or can be determined from the flowfield solution. The determination of the specific enthalpy of in-depth solid Teflon (h_i) with a consistent datum (reference) is very important and requires an accurate accounting of the physics of the Teflon surface ablation process.

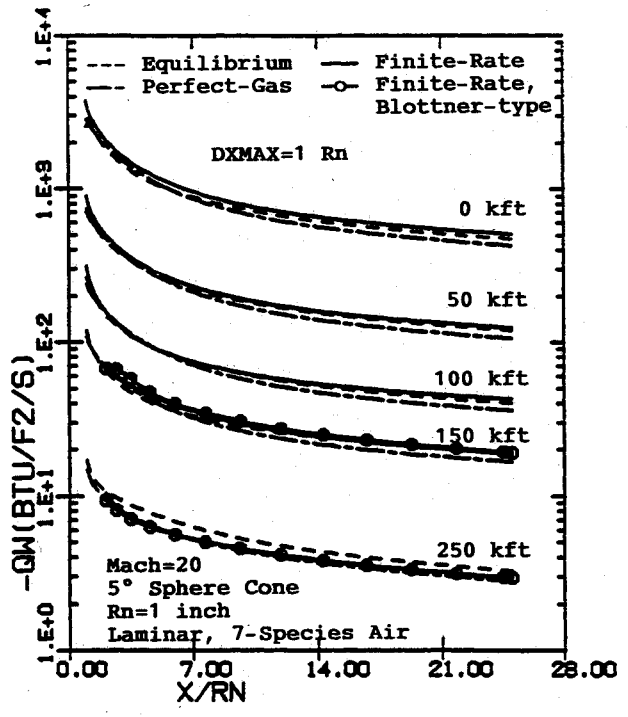

Fig. 6 Comparison of predicted wall heat-transfer rate for case 3.

Estimate of In-Depth Specific Enthalpy of Solid Teflon

Teflon (polytetrafluoroethylene) is a product of tetrafluoroethylene polymerization, possessing the chain $(C_2F_4)_n$ with a high degree of symmetry.[39] When subjected to intensive heating, depolymerization reaction of the Teflon polymer occurs. A good description of this depolymerization process has been given by Clark,[40] Holzknecht,[37] and Arai.[38] The data and descriptions given by these authors are quite similar; however, in what follows we will mostly use the notation and terminology used by Clark.[40] Briefly speaking, Teflon remains a white (partially crystalline) solid as long as its temperature is below 1080°R.[40] At this temperature (T_m), crystalline Teflon goes through a phase change process that is very similar to melting (thus, commonly called the melting point). This phase change is accompanied by a heat absorption of 25.2 Btu/lbm that is called either the heat of transition (H_m)[37-40] or, more appropriately, the latent heat of fusion (ΔH_f).[41] Above this melting temperature (T_m), Teflon is clear and amorphous and behaves like a gel.[40] At temperatures well above T_m, the Teflon polymer gel depolymerizes into a monomer that has a very high vapor pressure and, thus, flashes directly into vapor.[40] We will call this temperature the ablation temperature (T_a) and assume that it is independently known (the literature[42] shows that this ablation temperature can vary over a range from 1400 to 2200°R). As far as Teflon's heat of depolymerization (ΔH_p) is concerned, the lumped depolymerization and vaporization process absorbs approximately 750 Btu/lbm of energy.[39,40] Although some studies[38,40] also include a temperature dependence of ΔH_p to account for the partial depolymerization effects, we believe that for the present wall-ablation model this is an unnecessary refinement.

Let us denote the net heat absorbed to change from solid (crystalline) Teflon at the in-depth temperature (T_i) to the gaseous monomer C_2F_4 at the ablation temperature (T_a) as ΔH_{c-g}. Then the expression for ΔH_{c-g} in appropriate units becomes

$$\Delta H_{c-g} = \int_{T=T_i}^{T=T_m} Cp_c(T)\, dT + \Delta H_f + \int_{T=T_m}^{T=T_a} Cp_a(T)\, dT + \Delta H_p \tag{27}$$

where subscript c is used for crystalline and subscript a is used for amorphous phases.

The specific enthalpy of gaseous monomer C_2F_4 at the ablation temperature is obtained from the data of Browne and Miller.[43] Let us denote this gaseous monomer enthalpy as h_f and the enthalpy of in-depth solid Teflon (at $T = T_i$) as h_i. Then, by definition,

$$h_i = h_f - \Delta H_{c-g} \tag{28}$$

where ΔH_{c-g} is defined in Eq. (27) and the in-depth temperature (T_i) is assumed to be 540°R (300 K). In this manner, we can calculate the specific enthalpy of in-depth Teflon (h_i) consistent with the datum used by Browne[28-30] in describing the specific enthalpy data of the various gaseous species involved in the reacting Teflon-air mixture.

Results and Discussion

Several test cases were considered to evaluate the present coupled-chemistry PNS scheme. Some important results of these calculations are summarized in the following sections.

Validation of the Equilibrium Limit of the Chemical System

To test the stability of our coupled-chemistry PNS scheme under true chemical equilibrium conditions, we did the coupled-matrix chemistry solution for the conditions of infinite rate. In this case the convection and diffusion terms in the coupled-chemistry solution drop out and one is left with a point matrix solution representing the equilibrium equations of the law of mass action.

Table 3a Equilibrium composition for clean air

Temperature, K	Method[a]	Species mass fractions[b] O2	N2	NO	NO+	N	O
2000	G-B	0.22868	0.76176	0.00788	—	0.00000	0.00168
	CPL	0.22827	0.76139	0.00866	0.00000	0.00000	0.00167
4000	G-B	0.00072	0.75369	0.00678	—	0.00831	0.23023
	CPL	0.00072	0.75337	0.00804	0.00002	0.00831	0.22955
6000	G-B	0.00000	0.15124	0.00046	—	0.61399	0.23431
	CPL	0.00000	0.15126	0.00064	0.00069	0.61356	0.23385

[a]The two methods used are G-B, Gordon and McBride,[44] and CPL, present coupled-matrix solution scheme.
[b]These species mass fractions are for an elemental composition of O = 0.23456 and N = 0.76544 and a pressure of 0.01 atm.

Table 3b Equilibrium composition for Teflon-air mixture

Species	Method[a]	Species mass fractions[b] for various fuel-to-mixture ratios, % 10	20	50	80	100
N2	G-B	0.68888	0.61234	0.38272	0.15309	—
	CPL	0.68888	0.61234	0.38272	0.15309	—
O2	G-B	0.17910	0.12365	<EPS	<EPS	—
	CPL	0.17909	0.12365	<E−20	<E−44	—
NO	G-B	0.00003	0.00002	<EPS	<EPS	—
	CPL	0.00003	0.00002	<E−15	<E−27	—
CF4	G-B	0.06756	0.13512	0.37173	0.69409	0.87990
	CPL	0.06767	0.13535	0.37211	0.70128	0.87538
COF2	G-B	0.03064	0.06129	0.10233	0.01476	—
	CPL	0.03047	0.06095	0.10178	0.01487	—
CO	G-B	<EPS	<EPS	0.07473	0.07490	—
	CPL	<E−11	<E−11	0.07473	0.08213	—
CO2	G-B	0.03374	0.06757	0.06848	0.00076	—
	CPL	0.03384	0.06769	0.06866	<E−11	—
F	G-B	0.00000	0.00000	0.00000	<EPS	<EPS
	CPL	<E−06	<E−06	<E−11	<E−14	<E−13
C	G-B	0.00000	0.00000	0.00000	0.06241 (solid)	0.12009 (solid)
	CPL	<E−70	<E−70	<E−38	0.06049 (C3)	0.11946 (C3)

[a]The two methods used are G-B, Gordon and McBride,[44] and CPL, present coupled-matrix solution scheme.
[b]These species mass fractions are for a pressure of 0.06805 atm and a temperature of 1000 K; EPS implies that the mole fraction was less that 5.0E − 06.

Nonablating (Clean-Air) Case

Table 3a shows our predictions of this coupled-matrix solution for a pressure of 0.01 atm and temperatures of 2000, 4000, and 6000 K. The corresponding predictions of the equilibrium composition using the free-energy minimization technique of Gordon and McBride[44] are also shown in this table. As we can see from these results, the present coupled-matrix solution scheme can indeed accurately predict the limiting case of equilibrium chemically reacting flows. The slight differences in some concentrations are primarily due to some differences in the rate data used in our chemistry model and the data used by Gordon and McBride.

Ablating (Teflon-Air) Case

Table 3b shows our predictions of this coupled-matrix solution for the case of varying amounts of Teflon ablation products (fuel-to-mixture ratio). In this case calculations of equilibrium mixtures were done for a pressure of 0.06805 atm at a temperature of 1000 K with 10, 20, 50, 80, and 100% fuel-to-mixture ratios. The corresponding predictions of the equilibrium composition using the free-energy minimization technique of Gordon and McBride[44] are also shown in this table. For the Gordon and McBride calculations, it should be noted that species with mole fractions less than 5×10^{-6} were automatically identified as trace and, thus, not considered. As we can see from these results, the present coupled-matrix solution scheme and the corresponding chemical model (reactions and species) used can indeed accurately predict the limiting case of equilibrium chemically reacting Teflon-air mixtures obtained using a free-energy minimization technique. The slight differences in some concentrations are again primarily due to some differences in the rate data used in our chemistry model and the data used by Gordon and McBride. Another important difference between the present calculations and the Gordon and McBride predictions for fuel-rich conditions is that the present predictions are strictly for a single-phase gas mixture, whereas the Gordon and McBride scheme can treat solid carbon (a two-phase system). At high fuel-to-mixture ratios (>50%), the Gordon-McBride predictions include large amounts of unburnt solid carbon (Table 3b), whereas the present gas model produces almost equal amounts of gaseous carbon (C_3).

Validation of the Finite-Rate Calculations (Cases 1 and 2)

Case 1: 12.84/7 Deg Bicone Calculations

The straight bicone configuration used in these comparisons was tested in the NASA Langley Expansion Tube Facility.[45] Present numerical predictions have been compared with the

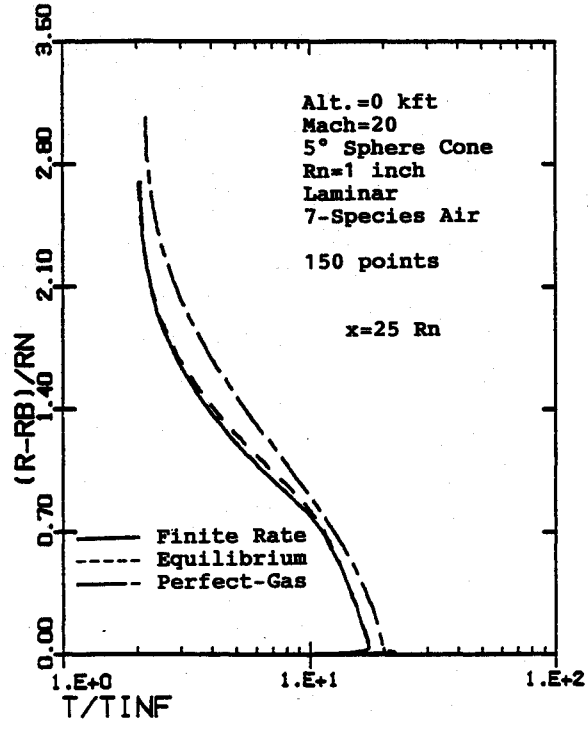

Fig. 7 Comparison of predicted temperature profiles at the body end for case 3 at sea level.

Table 4 Computing times for cases 1 and 2

Case	Altitude, kft	Mach no.	Data used[a]	Gas model[b]	DXMAX, Rn	Grid,[c] $N3 \times N2 \times N1$	Time, s[d]
1a	120	19.25	U-B	2-S	0.5	$1 \times 100 \times 77$	39
1b	120	19.25	U-B	2-S	0.5	$1 \times 150 \times 77$	71
1c	120	19.25	U-B	2-S	0.1	$1 \times 100 \times 309$	111
1d	120	19.25	EUK	2-S	0.5	$1 \times 100 \times 77$	37
1e	120	19.25	U-B	Diag	0.5	$1 \times 100 \times 77$	38
1f	120	19.25	U-B	S-I	0.5	$1 \times 100 \times 77$	41
2a	—	6.89	U-B	2-S	1.0	$1 \times 100 \times 1389$	315
2b	—	6.89	EUK	2-S	1.0	$1 \times 100 \times 1389$	300

[a]U-B = Uribe et al.[28] and Biolsi[29] thermal conductivity data with variable binary Lewis number, EUK = Eucken thermal conductivity approximation with a constant binary Lewis number of 1.4.
[b]2-S = two-step, Diag = diagonalized, S-I = strongly implicit.
[c]$N1$, $N2$, and $N3$ are the number of grid points in the streamwise, axis-normal, and crossflow directions, respectively.
[d]Computing times on Cray Y-MP with CFT77 compiler and autovectorization.

Table 5 Freestream conditions for cases 1 and 2

Quantity	Cases 1	Cases 2
W-T/Flight[a]	W-T	Flight
Mach number	6.89	19.25
Altitude, kft	—	120.00
Pressure, psf	45.57	9.585
Temperature, °R	2887.2	435.6
Wall-temperature range, °R	545–700	650–860
Flow type	laminar	laminar
Nose radius, in.	0.151	0.114

[a]W-T = wind-tunnel conditions, Flight = flight conditions.

available experimental data on the surface heat-transfer rates and also with our earlier equilibrium-air and perfect-gas predictions for these conditions.[12] The test configuration corresponds to a 12.84/7 deg bicone with a 0.151-in. nose radius (Rn), an $18.14Rn$ long forecone, and an overall body length of $31.88Rn$. The freestream conditions for this case are given in Table 4 and correspond to the Mach 6.89 flow at zero angle of attack. The clean air flow conditions were assumed to be fully laminar, and fully catalytic wall boundary conditions were used.

As expected, the predictions of the three nonequilibrium coupled-chemistry solution schemes used (diagonalized, two-step, and strongly implicit) were identical for all cases, and thus results are shown only for the two-step scheme. The effects of axis-normal and axial grid refinement are shown in Fig. 2, which shows that the heat-transfer predictions using DXMAX of $0.5Rn$ and $0.1Rn$ differed by less than 1%. This clearly suggests that DXMAX = $0.5Rn$ is indeed an adequate choice for resolving various geometry and flowfield features. The axis-normal grid refinement shows no difference between the 100- and 150-point predictions. These grid refinement studies not only show the fine-grid and small-step-size capabilities of our PNS scheme but also show that the present predictions are effectively grid independent.

According to Miller et al.,[45] the uncertainty in the heat-transfer data is about ±15%. In the forecone region the present nonequilibrium predictions and the data are in excellent agreement (Fig. 2). In the aftcone region the predictions are approximately 15% lower than the data but are still within the data uncertainty (Fig. 2). Under these conditions, the perfect-gas model underpredicts[12] the surface heating rates by as much as 40% in the forecone region and by approximately 25% in the aftcone region (Fig. 3). The present predictions agree with the previous computational results of Miller et al.[45] and Bhutta and Lewis[12] in being lower than the data in the aftcone region.

Figure 3 also shows the effects of transport property data on the predicted surface heat-transfer rates. The mixture Prandtl number (Pr) and mixture thermal conductivity ($\bar{k}$) profiles at the body end using the Eucken formula and our thermal-conductivity curvefits are shown in Fig. 4. This figure shows that in the outer region the Eucken formula underpredicts the mixture thermal conductivity by as much as 17% and, consequently, overpredicts the mixture Prandtl number by as much as 14%. These are significant changes that affect the overall temperature profiles and, thus, the surface heat-transfer rates by as much as 10% (Fig. 3). An important conclusion drawn from these results is that in resolving differences of the order of 10% in the predicted heat-transfer rate, the impact of the transport property data on nonequilibrium flowfield calculations cannot be neglected. Furthermore, the effects of diffusion modeling on nonequilibrium-air flowfield calculations seem to be insignificant compared with the overall effects of the species thermal conductivity data. The Cray Y-MP computing times and grids used for these cases are shown in Table 4. These times show that, in general, changing the grid size in the axial and axis-normal directions has almost a proportional effect on the final computing times.

Case 2: Laminar Re-Entry-F Calculations

The data[46] from the Re-entry-F flight experiment (1968) have been recently made available. This flight experiment

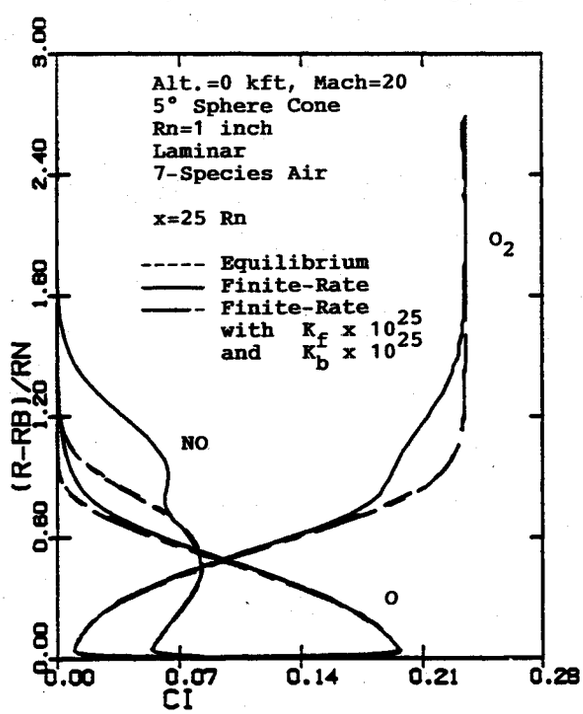

Fig. 8 Comparison of predicted species concentration profiles at the body end for case 3 at sea level.

involved the accurate measurement of surface heating rates on a long, slender conical re-entry vehicle (RV) under laminar, transitional, and turbulent flow conditions.[46] The particular RV consisted of a 5-deg half-angle sphere-cone with an overall length of 13 ft and an initial nose radius of 0.1 in. In this case we only considered the laminar, zero angle-of-attack data at 120 kft and assumed the wall to be fully catalytic. Equilibrium-air calculations for these conditions have been done by Thompson et al.[47] using a viscous shock layer scheme and by Bhutta and Lewis[12] using a PNS scheme. The freestream conditions for this case are shown in Table 5. The Mach number at this altitude was 19.25 and the Rn was 0.114 in.[46,47] In this case the grids used consisted of 100 points between body and the shock and DXMAX = 1Rn. Our earlier study[12] has shown that for this case this grid size is quite adequate for accurately resolving the flowfield as well as near-wall gradients.

The predicted axial distributions of surface heat-transfer rate for these calculations are shown in Fig. 5, which shows that the present nonequilibrium-air predictions are in close agreement with the flight data. In general, the results show that the nonequilibrium-air predictions are approximately 5% lower than the equilibrium-air predictions.[12] However, these differences are less than some of the variations in observed data, indicating that the predictions are probably well within the data uncertainty bounds. Figure 5 also shows that the improved species thermal conductivity data affects the predicted surface heat-transfer rate by approximately 5% and improves the agreement with the flight data. The computing times for this case are summarized in Table 4 along with the grid size used.

Five-Deg Sphere-Cone Calculations Without Surface Ablation (Case 3)

To investigate the stability, accuracy, and computational efficiency of our coupled-chemistry nonequilibrium PNS scheme, we studied the Mach 20 flow over a 5-deg sphere-cone vehicle for an altitude range of zero to 250 kft. The vehicle considered was 25 in. long with a 1-in. nose radius. The wall temperature was assumed to be fixed at 2000°R, and only laminar conditions were considered. Calculations were done at altitudes of 0, 10, 25, 50, 100, 150, and 250 kft with a seven-

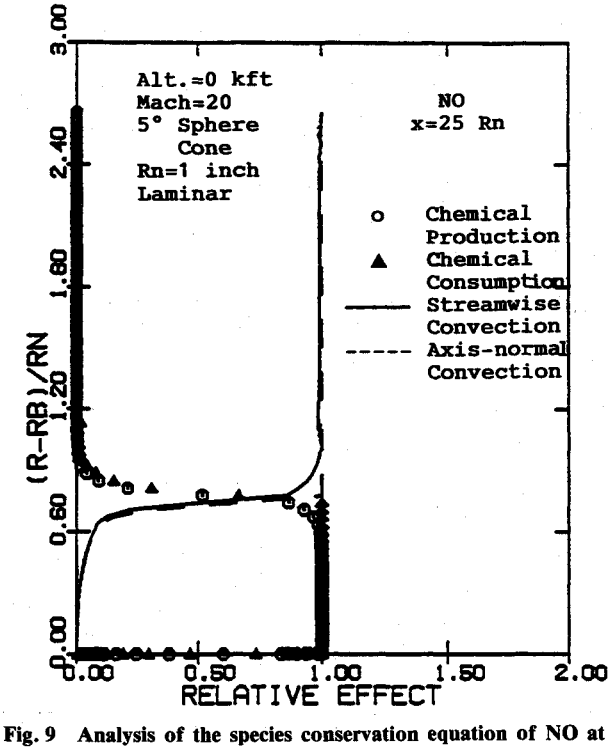

Fig. 9 Analysis of the species conservation equation of NO at the body end for case 3 at sea level.

Table 6 Computing times for various case 3 calculations

Case	Altitude, kft	Computing times[a,b] 2-S,[c] s	Diag,[c] s	S-I,[c] s	BLT,[c] s	EQ,[c] s	PG,[c] s
3a	250	13	13	14	13	5	4
3b	150	16	15	17	13	4	3
3c	100	23	24	24	—	4	3
3d	50	19	22	20	—	4	3
3e	25	19	32	20	—	4	3
3f	10	19	44	20	—	4	3
3g	0	19	48	20	—	4	3

[a]Computing times on Cray Y-MP with CFT77 compiler and autovectorization. [b]These solutions use the thermal conductivity data of Uribe et al.[28] and Biolsi[29] with a variable binary Lewis number and 100 points between the body and the shock.
[c]2-S = two-step, Diag = diagonalized, S-I = strongly implicit, BLT = Blottner-type linearization of production terms, EQ = equilibrium-air, PG = perfect gas.

Table 7 Effects of number of species on computing times

Number of species, NS	Altitude, ft	Computing times[a,b] 2-S,[c] s	Diag,[c] s	S-I,[c] s
Clean air, NS = 7	50	19	22	20
Teflon-air, NS = 23	50	41	47	156

[a]Computing times on Cray Y-MP with CFT77 compiler and autovectorization. [b]These solutions use the thermal conductivity data of Uribe et al.[28] and Biolsi[29] with a variable binary Lewis number and 100 points between the body and the shock. No surface blowing.
[c]2-S = two-step, Diag = diagonalized, S-I = strongly implicit.

Table 8 Computing times for various case 4 calculations

Case	Altitude, kft	Computing times[a] Grid,[b] $N1 \times N2$	DXMAX, Rn	CPU,[c] s
4a	250	56 × 100	0.5	93
4b	150	56 × 100	0.5	103
4c	100	64 × 100	0.5	145
4d	75	66 × 100	0.5	141

[a]These solutions use the thermal conductivity data of Uribe et al.[28] and Biolsi[29] with a variable binary Lewis number and the two-step solution scheme. Wall ablation is modeled using our coupled quasisteady ablation model.
[b]$N1$ and $N2$ are the number of axial and axis-normal grid points, respectively.
[c]Computing times on Cray Y-MP with CFT77 compiler and autovectorization.

species nonequilibrium-air gas model using the diagonalized, two-step, and strongly implicit solution schemes. Nonequilibrium-air calculations using the classical Blottner-type linearization of production terms were also attempted to access its stability characteristics. At all of these altitudes, additional calculations were also done using equilibrium-air and perfect-gas models.

For altitudes higher that 100 kft the PNS starting solutions were generated using a nonequilibrium VSL scheme, and the nonequilibrium afterbody calculations were done using a frozen shock crossing along with fully catalytic wall boundary conditions. For altitudes $\leq$ 100 kft the nose flowfield was assumed to be in equilibrium. In this case the PNS starting solutions were generated using an equilibrium-air VSL blunt-body scheme, and the subsequent nonequilibrium afterbody calculations were done using an equilibrium shock-crossing and equilibrium-catalytic wall boundary conditions. For altitudes $\leq$ 50 kft the PNS solutions were done using 100 as well as 150 points between the body and the shock, whereas for altitudes $>$50 kft only 100-point solutions were done. Comparison of these 100- and 150-point results showed that the wall heat-transfer predictions differed by less that 2%.

Table 6 shows the various solutions performed using different gas models and solution schemes over the altitude range from 0 to 250 kft and gives a summary of the grids used and the computing times required. This table, in fact, also shows some of the important results of this study. First of all it was observed that the classical Blottner-type[18] linearization of the production terms was only stable under high-altitude (>100 kft) nonequilibrium conditions. At 100 kft, it was unstable in the blunt-body region and was only marginally stable in the afterbody region. For altitudes lower than 100 kft, the Blottner-type[18] linearization was completely unstable.

On the other hand, the present coupled-chemistry formulation was stable over the entire altitude range from 0 to 250 kft. However, the observed stability characteristics of the three solution schemes tested were quite different. The convergence characteristics of the diagonalized formulation were quite sensitive to altitude variations, whereas the two-step and strongly implicit formulations had a more uniform behavior. At the highest altitude tested (250 kft), the diagonalized scheme was the most efficient, taking approximately 2% less computing time than the two-step and approximately 10% less time than the strongly implicit schemes. However, at the lowest altitude tested (sea level) the diagonalized scheme took approximately 2.5 times the computing times for the two-step and strongly implicit schemes. This is quite understandable because under high-altitude nonequilibrium conditions the mutual species coupling effects are relatively less important, and the resulting species conservation equations are very strongly diagonally dominant. But under low-altitude near-equilibrium conditions, the mutual species coupling effects (representing the off-diagonal coupling of the species conservation equations) are very important, and thus the diagonalized scheme is no longer strongly convergent and requires several more iterations to converge.

Although Table 6 shows that the two-step and strongly implicit schemes took nearly the same amount of computing time, it is only true because the number of species involved is small. In general, we expect the computing times for the two-step scheme to increase almost linearly with the number of species, whereas the computing time for the strongly implicit scheme will increase almost quadratically with the number of species. For ablative re-entry flowfields, the number of species is typically very large so that the difference between the computing time requirements of the two-step and strongly implicit schemes can be quite large. For example, Table 7 shows the corresponding computing times at 50 kft conditions using a 7-species nonequilibrium-air and a 23-species Teflon-air gas model. The surface is assumed to be nonablating so that the only difference between the two calculations is the number of chemical species, which increases by more than a

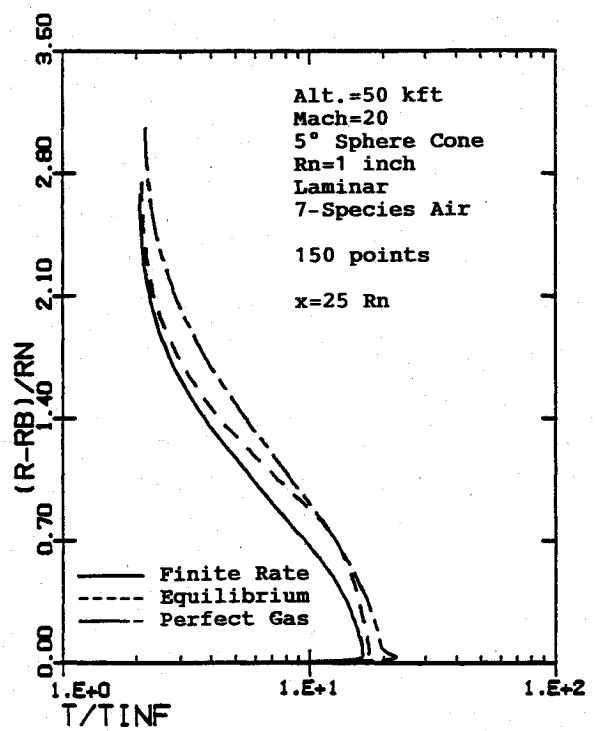

Fig. 10 Comparison of predicted temperature profiles at the body end for case 3 at 50 kft.

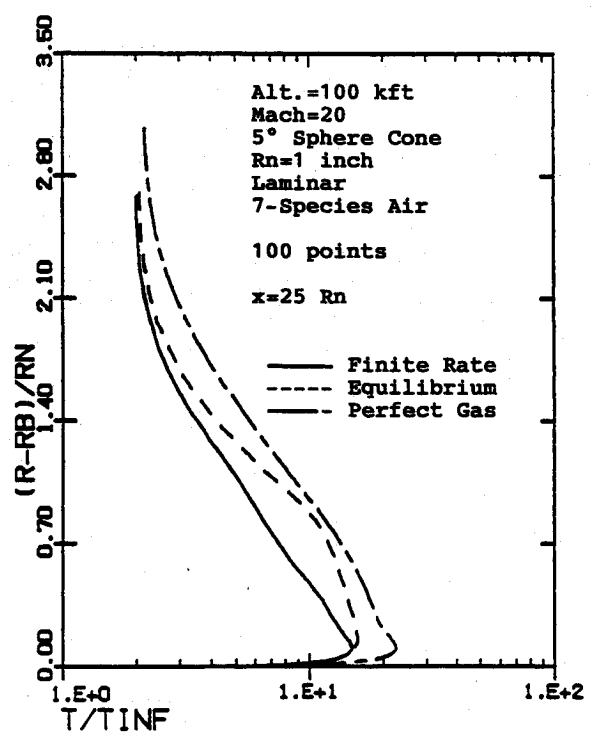

Fig. 11 Comparison of predicted temperature profiles at the body end for case 3 at 100 kft.

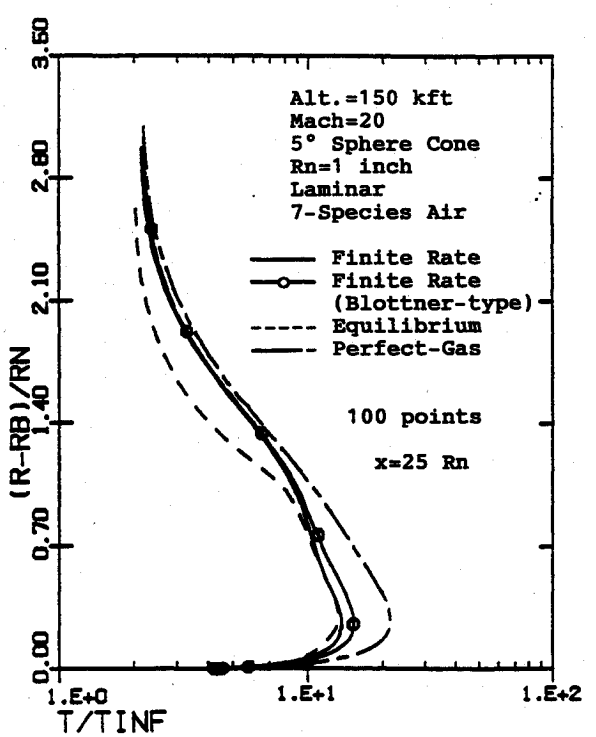

Fig. 12 Comparison of predicted temperature profiles at the body end for case 3 at 150 kft.

factor of 3 in going from the clean-air to the Teflon-air case. For the two-step scheme, the required computing times increase by a factor of 2, whereas in the strongly implicit case the required computing times increase by a factor of 8. These results clearly show that the present two-step scheme not only provides numerical stability comparable to the strongly implicit scheme and far superior to the stability characteristics of either the diagonalized scheme or a classical Blottner-type[21] linearization of the species production terms (Table 6), but it is also computationally the most efficient (Table 7), especially when the number of chemical species involved is large.

Figure 6 shows the surface heat-transfer rate for the nonequilibrium-air, equilibrium-air, and perfect-gas models at 0, 50, 100, 150, and 250 kft. For the sea level case, the equilibrium-air predictions are approximately 5% lower than the nonequilibrium-air predictions, whereas the perfect-gas predictions are approximately 20% lower (Fig. 6). The corresponding temperature profiles at the body end are compared in Fig. 7 and show that predictions of the equilibrium-air and nonequilibrium-air calculations are in close agreement, whereas the perfect-gas shock-layer temperatures are approximately 15% higher. The shock-layer thickness predicted by the equilibrium-air and nonequilibrium-air calculations are almost identical, whereas the perfect-gas model predicts a 14% thicker shock layer.

Although the surface heat-transfer rate (Fig. 6) and temperature profile (Fig. 7) predictions of the equilibrium-air and nonequilibrium-air gas models at sea level are quite close, there are some interesting features of the species profiles that are different. The O, NO, and O_2 mass-fraction profiles at the body end for the equilibrium and nonequilibrium calculations at sea level are shown in Fig. 8. This figure shows that the equilibrium and finite-rate predictions are almost identical in the initial 25% of the shock-layer region near the wall. In 25–75% of the shock-layer region there are significant differences in the equilibrium and finite-rate predictions, with the finite-rate calculations predicting higher concentrations of O and NO and lower concentrations of O_2. In the remaining 25% of the shock layer, the equilibrium and finite-rate predictions are almost identical and consist of primarily O_2 and N_2. For a clearer understanding of these results, we analyzed the

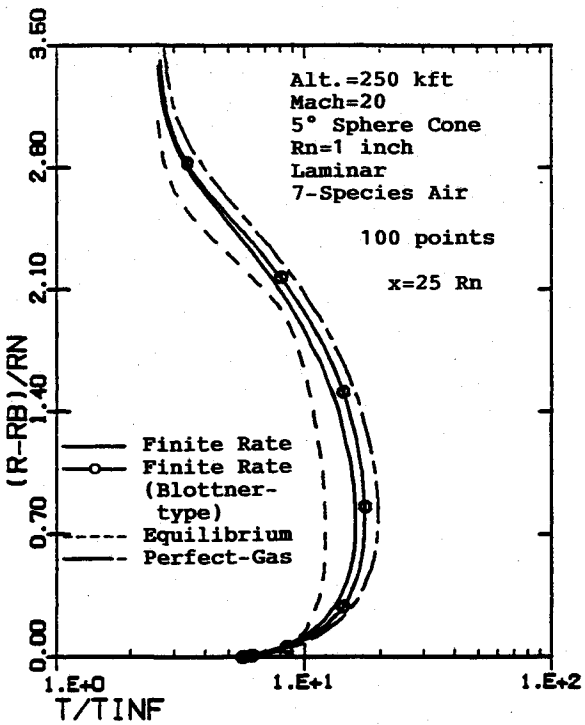

Fig. 13 Comparison of predicted temperature profiles at the body end for case 3 at 250 kft.

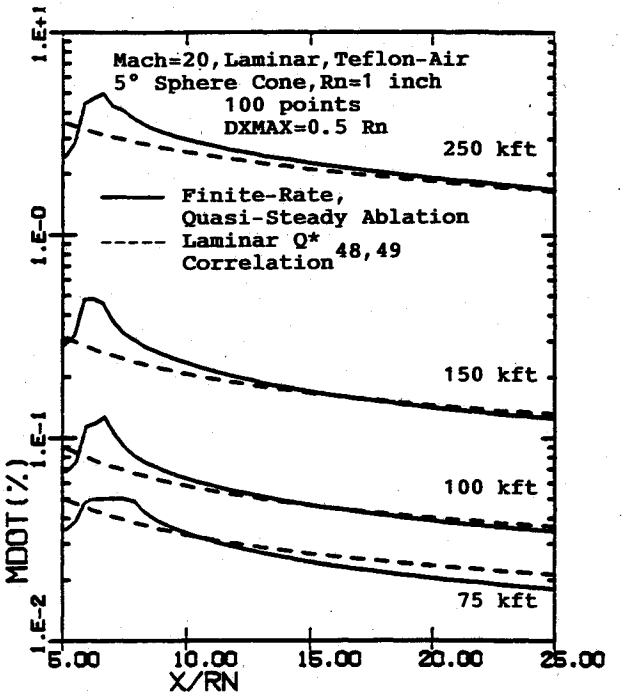

Fig. 14 Comparison of predicted surface ablation rate for case 4.

conservation equations for NO in detail across the shock layer. At each grid point, this species conservation equation was split into 1) the streamwise convections terms, 2) the axis-normal species convection terms, 3) the species diffusion terms, 4) the local production due to chemical reactions, and 5) the local consumption due to chemical reactions.

Figure 9 shows these terms (scaled with respect to the maximum term) across the shock-layer at the body end that shows that for these calculations the initial 25% of the shock-layer region near the wall is dominated by a balance between the chemical production and consumption terms; i.e., the flow is indeed in chemical equilibrium. In the subsequent 25–50% of the shock-layer region, the shock-layer temperature drops (see Fig. 7), and the chemical production/consumption terms rapidly become small whereas the species convection terms rapidly increase in importance. It is exactly this region where the effects of finite-rate chemistry are important, and the flow is not in equilibrium as shown by the species profiles in Fig. 8. In the remaining portion of the shock layer leading up to the shock, the chemical production/consumption effects are insignificant compared with the convection/diffusion effects, and thus the flow is frozen. In this case the temperature behind the shock is approximately 575 K, at which temperature the equilibrium limit is the same as the frozen limit consisting primarily of O_2 and N_2. This explains why the predicted nonequilibrium-air and equilibrium-air species profiles agree in the near-wall region, differ in the intermediate region away from the wall, and again start to agree in the outer region behind the shock. To further confirm these effects of finite-rate chemistry, we artificially increased the forward and backward reaction rates by a factor of 10^{25} to simulate the infinite-rate (equilibrium) limit. Figure 8 also shows the subsequent predictions of the species concentrations across the layer and shows that in the infinite-rate limit the nonequilibrium-air and equilibrium-air predictions indeed become identical. Thus, the observed differences between the equilibrium-air and nonequilibrium-air predictions of Fig. 8 are indeed due to the finite-rate chemistry effects.

The nonequilibrium-air, equilibrium-air, and perfect-gas predictions of the temperature profiles at 50 and 100 kft are shown in Figs. 10 and 11. In both cases the surface heat-transfer predictions of the equilibrium-air and nonequilibrium-air

gas models are within 5% of each other, whereas the perfect-gas predictions are approximately 20% lower (see Fig. 6). The temperature profiles show that the nonequilibrium-air and equilibrium-air predictions agree better in the near-wall region and the region behind the shock, whereas in between they differ from each other, reflecting the effects of nonequilibrium (finite-rate) chemistry. The corresponding temperature profiles across the shock-layer for the higher altitudes of 150 and 250 kft are shown in Figs. 12 and 13. In this case comparisons were also made with the corresponding predictions of our earlier nonequilibrium-air PNS scheme using $Le = 1.4$ and a Blottner-type[18] linearization of the species production, and the agreement was found to be very good under these nonequilibrium conditions. In general, these results show that at high altitudes the nonequilibrium predictions tend to approach the perfect-gas predictions (Figs. 12 and 13), whereas at low altitudes they tend to approach the equilibrium-air predictions (Figs. 10 and 11).

Five-Deg Sphere-Cone Calculations with Surface Ablation (Case 4)

The 5-deg sphere-cone configuration of case 3 was also studied with an ablating Teflon surface model for the afterbody region. In this case the forebody ($x \leq 5Rn$) was assumed to be nonablating whereas the afterbody ($x > 5Rn$) was assumed to have an ablating Teflon surface. Teflon surface-ablation effects were modeled using our quasisteady model that was coupled to the local flowfield calculations. Only laminar flow conditions were considered, and calculations were done for altitudes of 250, 150, 100, and 75 kft. The freestream Mach number was assumed to be 20, and the wall temperature was kept fixed at 2000°R.

In this case only 100 points were used between the body and the shock along with a DXMAX of $0.5Rn$. For the 150 and 250 kft conditions, the initial starting solutions were generated using a nonequilibrium VSL scheme, and the afterbody solutions were done using a frozen shock crossing. The wall boundary conditions were assumed to be fully catalytic for the nonablating region and equilibrium-catalytic for the ablating afterbody region. For the 75 and 100 kft cases, the initial starting solutions were generated using an equilibrium-air VSL scheme, and the afterbody solutions used equilibrium shock crossing and equilibrium-catalytic wall boundary conditions for the ablating as well as the nonablating regions.

In this case we also used the laminar Q^* model of Scala[48] to predict the Teflon surface-ablation rates to be expected at these altitudes. This is an empirical correlation that was developed from available data on various types of re-entry configurations. This correlation uses the no-blowing cold-wall heat-transfer rate along with the wall pressure to predict the local ablation rate.[48,49] We used our no-blowing perfect-gas PNS calculations of case 3 to obtain these quantities and, thus, the expected axial distribution of the Teflon surface-ablation rate.

The final converged Teflon surface-ablation rates at each marching step using our coupled-chemistry scheme and our quasisteady Teflon ablation model are shown in Fig. 14. This figure also includes the corresponding predictions of the laminar Q^* correlation of Scala[48] and Brant.[49] These results show that, for all the altitudes considered, the present quasisteady ablation predictions are within 10% of the predictions of the laminar Q^* model. This is exceptionally good agreement and not only is a measure of the accuracy of our new quasisteady Teflon-ablation model but also reflects the accuracy of the associated wall heat-transfer and flowfield predictions for the complex finite-rate chemically reacting Teflon-air model.

For these cases with ablation, the onset of ablation at $x = 5$ Rn is accompanied by the sudden development of large near-wall gradients of the ablation products that initially increase rapidly because the concentrations of the ablation products at the wall increases. Consequently, the diffusion heat transfer to the surface increases, which causes the predicted surface-ablation rate to increase (Fig. 14). However, as we move further downstream, the direct effects of surface ablation (blowing) become more pronounced, and thus the total wall heat-transfer rate and the associated surface-ablation rate decrease (Fig. 14).

For the 75 and 100 kft cases, there are significant surface ablation effects and the mass-fraction of fuel (C, F, and Na) at the wall is more than 60%. In general, the distributions across the layer are quite smooth, with the Teflon-air mixture becoming rapidly lean as we move away from the wall.

For these calculations only the two-step solution scheme was used, and the corresponding computing times are shown in Table 8. Compared with the sample nonablating Teflon-air calculation at 50 kft (Table 7), we see that the required computing times for the cases with ablation are on the average 3.5 times more. This is primarily because the axial step sizes used are about 1.5 times smaller, and the number of iterations per marching step is approximately a factor of 2 larger than the corresponding nonablating case. In this study no attempt was made to optimize the iteration strategy (underrelaxation, initial guess, etc.) for the ablating cases to reduce the number of iterations required. However, appropriate strategies can easily be developed to further reduce the number of iterations and, thus, substantially reduce the overall computing time required.

Conclusions

A new coupled-chemistry PNS scheme has been developed to study hypersonic re-entry flows over the entire range of frozen, nonequilibrium, near-equilibrium, and equilibrium chemically reacting flows over multiconic RVs with nonablating and ablating Teflon surfaces. This coupled solution scheme can use either a strongly implicit or a two-step solution approach, and the technique has been used to study the hypersonic flow over various configurations over a Mach number range of 6.89–20 and for the entire altitude range from sea level to 250 kft. The results of this study substantiate the following comments:

1) Based on the axisymmetric PNS scheme of Bhutta and Lewis,[1-12] a new coupled-chemistry PNS solution scheme has been developed that is stable over the entire range of frozen, nonequilibrium, near-equilibrium, and equilibrium flow conditions. The basic PNS scheme used is unconditionally timelike in the subsonic as well as the supersonic flow regions and does not require the use of any sublayer approximation.

2) The results of the various test cases considered show that the new strongly implicit, two-step, and diagonalized coupled-chemistry PNS schemes developed in this study are indeed stable under nonequilibrium as well as equilibrium flow conditions.

3) In the nonequilibrium limit, the flowfield and chemistry predictions of the new coupled-chemistry scheme are in excellent agreement with our existing uncoupled nonequilibrium PNS scheme. In the equilibrium limit, the flowfield and chemistry predictions of this coupled-chemistry scheme are in excellent agreement with the predictions of our existing equilibrium-air PNS scheme.

4) The low-altitude high-Mach-number flowfield calculations show that in the afterbody only the near-wall region is in equilibrium, whereas the remaining shock-layer region shows significant effects of finite-rate chemistry.

5) In general, the results show that the new two-step coupled-chemistry solution scheme for the species conservation equations provides a unique combination of efficiency, accuracy, and numerical stability over the entire range of equilibrium, near-equilibrium, and nonequilibrium flows involving complex chemical systems.

6) The results of this study indicate that reliable, accurate, and efficient nonequilibrium PNS afterbody schemes can be developed to predict hypersonic reentry flowfields over BRV/MaRV/Decoy configurations with complex chemistry and sur-

face ablation effects over the entire altitude range of sea level to 250 kft.

Acknowledgments

The work reported in this paper was supported in part by the NASA Lewis Research Center under Contract NAS3-25450. The encouragement and cooperation provided by Louis Povinelli, Dan Whipple, and the contract monitor Tom Benson during the course of this effort are gratefully acknowledged. The authors would also like to thank James E. Daywitt and Darius N. Brant of GE Re-entry Systems Department, Philadelphia, for their valuable suggestions about Teflon ablation modeling and their help in obtaining the Re-entry-F flight data.

References

[1]Bhutta, B. A., and Lewis, C. H., "Low Reynolds Number Flows Past Complex Multiconic Geometries," AIAA Paper 85-0362, Jan. 1985.

[2]Bhutta, B. A., Lewis, C. H., and Kautz, F. A., II, "A Fast Fully-Iterative Parabolized Navier-Stokes Scheme for Chemically-Reacting Reentry Flows," AIAA Paper 85-0926, June 1985.

[3]Bhutta, B. A., and Lewis, C. H., "Three-Dimensional Hypersonic Nonequilibrium Flows at Large Angles of Attack," *Journal of Spacecraft and Rockets,* Vol. 26, No. 3, 1989, pp. 158–166; see also AIAA Paper 88-2568, June 1988.

[4]Bhutta, B. A., and Lewis, C. H., "Prediction of Nonequilibrium Viscous Hypersonic Flows over Lifting Configurations," AIAA Paper 89-1696, June 1989.

[5]Bhutta, B. A., and Lewis, C. H., "Three-Dimensional Parabolized Navier-Stokes Predictions of Hypersonic Nonequilibrium Flows over Ablating Teflon Surfaces," Vol. I: Technical Report, Vol. II: User's Manual, VRA, Inc., VRA-TR-87-02, Blacksburg, VA, Dec. 1987.

[6]Bhutta, B. A., Song, D. J., and Lewis, C. H., "Nonequilibrium Viscous Hypersonic Flows over Ablating Teflon Surfaces," *Journal of Spacecraft and Rockets,* Vol. 27, No. 2, 1990, pp. 205–215; see also AIAA Paper 89-0314, Jan. 1989.

[7]Bhutta, B. A., and Lewis, C. H., "An Implicit Parabolized Navier-Stokes Scheme for High-Altitude Reentry Flows," AIAA Paper 85-0036, Jan. 1985.

[8]Bhutta, B. A., and Lewis, C. H., "PNS Predictions of Three-Dimensional Hypersonic Flows with Strong Crossflow Effects," *Journal of Thermophysics and Heat Transfer,* Vol. 4, No. 1, 1990, pp. 27–36; see also AIAA Paper 88-2696, June 1988.

[9]Bhutta, B. A., and Lewis, C. H., "Large Angle-of-Attack Viscous Hypersonic Flows over Complex Lifting Configurations," *Journal of Spacecraft and Rockets,* Vol. 27, No. 2, 1990, pp. 194–204; see also AIAA Paper 89-0269, Jan. 1989.

[10]Bhutta, B. A., and Lewis, C. H., "Prediction of Three-Dimensional Hypersonic Flows Using a Parabolized Navier-Stokes Scheme," *Journal of Spacecraft and Rockets,* Vol. 26, No. 1, 1989, pp. 4–13; see also AIAA Paper 85-1604, July 1985.

[11]Bhutta, B. A., and Lewis, C. H., "Prediction of Axisymmetric Hypersonic Blunt-Body Flows Using a Parabolized Navier-Stokes Scheme," AIAA Paper 89-1831, June 1989.

[12]Bhutta, B. A., and Lewis, C. H., "Comparison of Hypersonic Experiments and PNS Predictions Part I: Aerothermodynamics," *Journal of Spacecraft and Rockets,* Vol. 28, No. 4, 1991, pp. 376–386; also AIAA Paper 90-3068, Aug. 1990.

[13]Finson, M. L., Ameer, P. G., Person, J. C., Cronin, J. F., and Parker, P. D., "Non-Equilibrium Boundary-Layer Code," Vol. I: Numerical Methodology, Vol. II: User's Manual, Physical Sciences, Inc., PSI-9030/TR-676, Andover, MA, June 1988.

[14]Widhopf, G. F., and Victoria, K. J., "On the Solution of the Unsteady Navier-Stokes Equations Including Multicomponent Finite Rate Chemistry," *Computers and Fluids,* Vol. 1, June 1973, pp. 159–184.

[15]Finson, M. L., and Ameer, P. G., "Non-Equilibrium Boundary-Layer Code," Physical Sciences, Inc., PSI-069/TR-512, Andover, MA, May 1985.

[16]Li, C. P., "Implicit Methods for Computing Chemically Reacting Flow," NASA TM 58274, Sept. 1986.

[17]Browne, W. G., "Thermodynamic Properties of Some Ablation Materials from Plastic Heatshields in Air," General Electric Co., Aerospace Physics Memorandum 11, Philadelphia, PA, March 1964.

[18]Blottner, F. G., Johnson, M., and Ellis, M., "Chemically Reacting Viscous Flow Program for Multi-Component Gas Mixtures," Sandia National Lab., Rept. SC-RR-70-754, Albuquerque, NM, Dec. 1971.

[19]Miner, E. W., and Lewis, C. H., "Hypersonic Ionizing Air Viscous Shock Layer Flows over Nonanalytic Blunt Bodies," NASA CR-2550, May 1975.

[20]Bortner, M. H., "Chemical Kinetics in a Re-Entry Flow Field," General Electric Co., TIS R63SD63, Philadelphia, PA, Aug. 1963.

[21]Cresswell, J., Kaplan, B., Porter, R., and Sarcos, C., "Material Effects of Low Temperature Ablators on Hypersonic Wake Properties of Slender Bodies," General Electric Co., TIS 67SD255, Philadelphia, PA, May 1967.

[22]Blottner, F. G., "Prediction of Electron Density in the Boundary Layer on Entry Vehicles With Ablation," *The Entry Plasma Sheath and Its Effects on Space Vehicle Electromagnetic Systems,* NASA SP-252, Vol. 1, Oct. 1970, pp. 219–240.

[23]Braun, E. R., "Effects of a Fully Catalytic Wall on a Nonequilibrium Boundary Layer Including Ablating Ablation Products," M.S. Thesis, Polytechnic Inst. of Brooklyn, Brooklyn, NY, June 1970.

[24]Modica, A. P., private communications, Textron Defense Systems, Wilmington, MA, April 1990.

[25]Browne, W. G., "Thermodynamic Properties of Some Atoms and Atomic Ions," General Electric Co., MSD Engineering Physics TM2, Philadelphia, PA.

[26]Browne, W. G., "Thermodynamic Properties of Some Diatomic and Linear Polyatomic Molecules," General Electric Co., MSD Engineering Physics TM3, Philadelphia, PA.

[27]Browne, W. G., "Thermodynamic Properties of Some Diatomic and Diatomic Ions at High Temperatures," General Electric Co., MSD Advanced Aerospace Physics TM8, Philadelphia, PA, May 1962.

[28]Uribe, F. J., Mason, E. A., and Kestin, J., "Thermal Conductivity of Nine Polyatomic Gases at Low Density," *Journal of Physical and Chemical Reference Data,* Vol. 19, No. 5, 1990, pp. 1124–1136.

[29]Biolsi, L., private communication, Univ. of Missouri-Rolla, Rolla, MO, Nov. 1987.

[30]Viviand, H., "Conservative Forms of Gas Dynamics Equations," *La Recherche Aerospatiale,* No. 1, 1974, pp. 65–68.

[31]Peyert, R., and Viviand, H., "Computations of Viscous Compressible Flows Based on the Navier-Stokes Equations," AGARD-AG-212, 1975.

[32]Bird, R. B., Stewart, W. E., and Lightfoot, E. N., *Transport Phenomena,* Wiley, New York, 1960.

[33]Davis, R. T., "Hypersonic Flow of a Chemically Reacting Binary Mixture past a Blunt Body," AIAA Paper 70-805, July 1970.

[34]Moss, J. N., "Solutions for Reacting and Nonreacting Viscous Shock Layers with Multicomponent Diffusion and Mass Injection," Ph.D. Dissertation, Virginia Polytechnic Inst. and State Univ., Blacksburg, VA, Oct. 1971.

[35]Swaminathan, S., Kim, M. D., and Lewis, C. H., "Three-Dimensional Nonequilibrium Viscous Shock-Layer Flows over Complex Geometries," *AIAA Journal,* Vol. 22, No. 6, 1984, pp. 754–755; see also AIAA Paper 83-0212, Jan. 1983.

[36]Thareja, R. R., Szema, K. Y., and Lewis, C. H., "Chemical Equilibrium Laminar or Turbulent Three-Dimensional Viscous Flows," *Journal of Spacecraft and Rockets,* Vol. 20, No. 5, 1983, pp. 454–460; see also AIAA Paper 82-0305, Jan. 1982.

[37]Holzknecht, B., "An Analytical Model of the Transient Ablation of Polytetrafluoroethylene Layers," *International Journal of Heat and Mass Transfer,* Vol. 20, June 1977, pp. 661–668.

[38]Arai, N., "Transient Ablation of Teflon in Intensive Radiative and Convective Environments," *AIAA Journal,* Vol. 17, No. 6, 1979, pp. 634–640.

[39]Luikov, A. V., Shashkov, A. G., and Yurevich, F. B., "Polytetrafluoro-Ethylene Ablation in High-Temperature Jet of Different Chemical Composition," *International Journal of Heat and Mass Transfer,* Vol. 12, 1969, pp. 635–643.

[40]Clark, B. L., "A Parametric Study of the Transient Ablation of Teflon," *Journal of Heat Transfer,* Vol. 94C, Nov. 1972, pp. 347–354.

[41]Settlage, P. H., and Siegle, J. C., "Behavior of 'Teflon' Fluorocarbon Resins at Elevated Temperatures," *Physical Chemistry in Aerodynamics and Space Flight,* Pergamon, New York, 1961.

[42]Kemp, N. H., "Surface Recession Rate of an Ablating Polymer," *AIAA Journal,* Vol. 6, No. 9, 1968, pp. 1790–1791.

[43]Browne, W. G., and Miller, J., "Thermodynamic Properties of Some Ablation Products from Teflon Heat Shields in Air," General Electric Co., Rept. 65SD5315, Philadelphia, PA, Oct. 1965.

[44]Gordon, S., and McBride, B. J., "Computer Program for Calculation of Complex Chemical Equilibrium Compositions, Rocket Per-

formance, Incident, and Reflected Shocks, and Chapman-Jouguet Detonations," NASA SP-273, March 1976.

[45]Miller, C. G., III, Micol, J. R., and Gnoffo, P. A., "Laminar Heat-Transfer Distribution on Biconics at Incidence in Hypersonic-Hypervelocity Flows," NASA TP 2213, Jan. 1985.

[46]Stainback, P. C., Johnson, C. B., Boney, L. B., and Wicker, K. C., "Comparison of Theoretical Predictions and Heat-Transfer Measurements for a Flight Experiment at Mach 20 (Reentry F)," NASA TM X-2560, 1972.

[47]Thompson, R. A., Zoby, E. V., Wurster, K. E., and Gnoffo, P. A., "An Aerothermodynamic Study of Slender Conical Vehicles," AIAA Paper 87-1475, June 1987.

[48]Scala, S. M., "A Study of Hypersonic Ablation," General Electric Co., GE-RESD TIS-R59SD438, Philadelphia, PA, Sept. 1959.

[49]Brant, D. N., "Investigation of Teflon Performance on the MK 12 Nosetip," General Electric Co., GE-RESD PIR-9151-AE-104, Philadelphia, PA, Dec. 1973.

Ernest V. Zoby
Associate Editor